The total satellite population of the Milky Way

Oliver Newton,[*] Marius Cautun, Adrian Jenkins, Carlos S. Frenk and John C. Helly
Institute for Computational Cosmology, Durham University, South Road, Durham, DH1 3LE, UK

ABSTRACT

The total number and luminosity function of the population of dwarf galaxies of the Milky Way (MW) provide important constraints on the nature of the dark matter and on the astrophysics of galaxy formation at low masses. However, only a partial census of this population exists because of the flux limits and restricted sky coverage of existing Galactic surveys. We combine the sample of satellites recently discovered by the Dark Energy Survey (DES) with the satellites found in Sloan Digital Sky Survey (SDSS) Data Release 9 (together these surveys cover nearly half the sky) to estimate the total luminosity function of satellites down to $M_V = 0$. We apply a new Bayesian inference method in which we assume that the radial distribution of satellites independently of absolute magnitude follows that of subhaloes selected according to their peak maximum circular velocity. We find that there should be at least 124^{+40}_{-27} (68 per cent CL, statistical error) satellites brighter than $M_V = 0$ within 300 kpc of the Sun. As a result of our use of new data and better simulations, and a more robust statistical method, we infer a much smaller population of satellites than reported in previous studies using earlier SDSS data only; we also address an underestimation of the uncertainties in earlier work by accounting for stochastic effects. We find that the inferred number of faint satellites depends only weakly on the assumed mass of the MW halo and we provide scaling relations to extend our results to different assumed halo masses and outer radii. We predict that half of our estimated total satellite population of the MW should be detected by the Large Synoptic Survey Telescope. The code implementing our estimation method is available online.[1]

Key words: Galaxy: halo – galaxies: dwarf – dark matter.

1 INTRODUCTION

Proposed in the 1980s (e.g. Peebles 1982; Davis et al. 1985), the Λ cold dark matter (ΛCDM) model has proved remarkably successful at predicting numerous observable properties of the Universe and their evolution over time; as a result, it has become the 'standard model' of cosmology (see Frenk & White 2012; Weinberg et al. 2015, for recent reviews). Hierarchical structure formation is fundamental to this model, which predicts that dark matter (DM) haloes form by mergers of smaller haloes and smooth mass accretion. Merged (sub)haloes that are not completely disrupted are detectable today as satellite galaxies and, potentially, as non-luminous substructures.

The Milky Way (MW) halo and its associated satellite galaxies offer an ideal environment in which to probe hierarchical growth which, in turn, can be used to constrain the faint end of galaxy formation and the properties of the DM. However, the current census of MW satellite galaxies is highly incomplete. The most recent

surveys – such as the Sloan Digital Sky Survey (SDSS; Alam et al. 2015) and the Dark Energy Survey (DES; Bechtol et al. 2015; Drlica-Wagner et al. 2015) – do not cover the entirety of the sky and are also subject to detectability limits that depend on the surface brightness of and distance to the satellite galaxies. The goal of this paper is to overcome some of these limitations and, using theoretical priors based on cosmological simulations of MW-like haloes, to estimate the expected total number of MW satellite galaxies.

In the 1990s, DM-only CDM simulations showed that many more subhaloes survive within MW-like haloes than there are visible satellites orbiting the MW (Klypin et al. 1999; Moore et al. 1999; Springel et al. 2008). This disparity is often referred to as the 'missing satellites problem for cold dark matter.' This rather unfortunate nomenclature is very misleading if, as is common usage, the word 'satellite' is taken to mean a visible galaxy: DM-only simulations have, of course, nothing to say about visible galaxies. Simple processes, at the heart of galaxy formation theory, such as the reionization of hydrogen in the early universe and supernovae feedback, make it impossible for visible galaxies to form in the vast majority of CDM haloes. Such processes were first discussed and calculated in this context using semi-analytic techniques with

[*] E-mail: oliver.j.newton@durham.ac.uk

[1]This is available from Newton & Cautun (2018).

different approximations in the early 2000s (Bullock, Kravtsov & Weinberg 2000; Benson et al. 2002a,b; Somerville 2002). For example, Benson et al. (2002a) showed how the abundance and stellar content of dwarf galaxies are driven by reionization and supernovae feedback. Their model produced an excellent match to the luminosity function of the (11 'classical' – the only known at the time) satellites of the MW and predicted that the MW halo should host a large population of fainter satellites. Just such a population was discovered several years later in the SDSS (Koposov et al. 2008, and references therein).

The early semi-analytic results have been confirmed using full hydrodynamic simulations (e.g. Okamoto et al. 2005; Macciò et al. 2007). For example, the most recent such simulations have confirmed that below a certain halo mass, typically $\sim 10^{10}\,\mathrm{M_\odot}$, dwarf galaxy formation is strongly suppressed, and that the majority of haloes with masses $\lesssim 10^9\,\mathrm{M_\odot}$ should not host a luminous component (stellar mass greater than $10^4\,\mathrm{M_\odot}$) (Shen et al. 2014; Sawala et al. 2015, 2016a; Wheeler et al. 2015).

In recent years, alternatives to CDM have elicited considerable interest. Some of these, such as Warm Dark Matter (WDM, Avila-Reese et al. 2001; Bode, Ostriker & Turok 2001), models with interactions besides gravity between DM particles and photons or neutrinos (Bœhm et al. 2014) and axionic DM (Marsh 2016), predict a cut-off in the primordial matter power spectrum on astrophysically relevant scales, which would suppress the formation of small galaxies (Bode et al. 2001; Polisensky & Ricotti 2011; Lovell et al. 2012; Schewtschenko et al. 2015). The abundance of the faintest galaxies can thus, in principle, reveal or rule out the presence of a power spectrum cut-off. By requiring that WDM models should produce at least enough substructures to match the observed Galactic satellite count, constraints on the mass and properties of the DM particle can be derived (Macciò & Fontanot 2010; Kennedy et al. 2014; Lovell et al. 2014; Schneider 2016; Bose et al. 2017; Lovell et al. 2017).

Past and current surveys have now discovered a plethora of satellites around the MW, with the count currently standing at 56: 11 classical satellites, 17 discovered in each of the SDSS and DES surveys, and 11 found in other surveys. Despite this relatively large number of known satellites, current estimates suggest that there could be at least a factor of 3–5 times more still waiting to be discovered (Koposov et al. 2008; Tollerud et al. 2008; Hargis, Willman & Peter 2014). These estimates were made prior to the DES and are based only on SDSS data. These predictions start from an assumed radial profile for the distribution of Galactic satellites: either that it follows the DM density profile – as in Koposov et al. (2008), which is not a good assumption – or that it follows the subhalo number density profile (as in the other studies cited above). Then, for each observed satellite, they calculate the number of satellites in the entire fiducial volume that must be present in order to have, on average, one object with the corresponding properties within the survey volume.

This paper improves upon previous estimates of the Galactic satellite count in three major ways. First, while previous studies were based on SDSS data alone, our result makes use of the combined SDSS and DES data, which together cover an area equivalent to nearly half of the sky. Secondly, to properly account for stochastic effects, we introduce a new Bayesian approach for estimating the total satellite count. Stochastic effects – which we find to be the leading cause of uncertainty – have been overlooked in previous studies, resulting in a significant underestimation of their errors. Finally, we make use of a set of five high-resolution simulated host haloes – taken from the AQUARIUS project (Springel et al. 2008) –

to characterize uncertainties arising from host-to-host variation. In 2016 December, Jethwa, Erkal & Belokurov (2018) presented a Bayesian estimate of the total number of Galactic satellites. Their result is the outcome of applying abundance matching to the SDSS observations and, while it properly accounts for stochastic effects, it depends on more and uncertain assumptions (mostly related to abundance matching) than the result presented here.

We organize this paper as follows. Section 2 introduces the observational data set used in this analysis and Section 3 describes, tests, and compares our Bayesian technique with previous works. We present our main results in Section 4, detailing their sensitivity to the assumed MW halo mass and the radial dependence of the satellite count. Section 5 discusses the implications of our results and considers some of the limitations of our method. We present concluding remarks in Section 6.

2 OBSERVATIONAL DATA

Very few of the current set of MW satellites were known prior to the start of the 21st century. Discoveries made after this time, using a multitude of techniques, together with data from SDSS data release 2 (DR2) and the Two Micron All-Sky Survey (2MASS) – before a major advance with SDSS DR5 (Adelman-McCarthy et al. 2007) – brought the total to 23 dwarf galaxies. Since then, the SDSS area has nearly doubled and DES is now electronically available. Combining the two surveys produces a sky coverage area of 47 per cent, with SDSS and DES contributing 14 555 and 5000 square degrees, respectively. An analysis of DES data added a further 17 dwarf galaxies to the running total (Bechtol et al. 2015; Drlica-Wagner et al. 2015; Kim et al. 2015; Koposov et al. 2015a), which, together with other discoveries, brings the total number of dwarf galaxies, as of 2018 February, to 56. These are listed in Tables A1 and A2 of Appendix A.

These discoveries resulted from the use of advanced search algorithms that comb through survey data and identify overdensities of stars which could signal the presence of a faint dwarf galaxy. For example, the SDSS has been analysed with two such search algorithms, by Koposov et al. (2008) and Walsh, Willman & Jerjen (2009), to find that both techniques recover the same number of dwarf galaxies – although the latter is sensitive to fainter objects. Each algorithm has a response function that – among other factors such as the survey surface brightness limits – is dependent on the absolute magnitude of the objects being searched for. Assuming isotropy, the number of observed satellites per unit magnitude, $\mathrm{d}N_{\mathrm{sat}}/\mathrm{d}M_{\mathrm{V}}$, is given by

$$\frac{\mathrm{d}N_{\mathrm{sat}}}{\mathrm{d}M_{\mathrm{V}}} = \int_0^\infty \int_0^\infty \Omega r^2 \frac{\mathrm{d}^3 N_{\mathrm{sat}}}{\mathrm{d}r\,\mathrm{d}M_{\mathrm{V}}\,\mathrm{d}r_{\mathrm{sat}}} \epsilon(r, M_{\mathrm{V}}, r_{\mathrm{sat}})\,\mathrm{d}r\,\mathrm{d}r_{\mathrm{sat}}, \qquad (1)$$

where the first integral is over the survey volume, with Ω the survey solid angle and r the radial distance from the Sun. The second integral is over the satellite size, r_{sat}; N is the distribution of satellites as a function of radial distance from the Sun, absolute magnitude, M_{V}, and size, r_{sat}. The last term, ϵ, denotes the efficiency of the search algorithm for identifying a satellite of magnitude, M_{V}, and size, r_{sat}, at distance, r, averaged over the survey's sky-footprint. At fixed absolute magnitude, most of the satellites detected in the SDSS have similar sizes and the detection efficiency, ϵ, is approximately equal for all objects (Koposov et al. 2008; Walsh et al. 2009). Thus, for the observed satellites, the dependence on r_{sat} in equation (1) can be approximated as a dependence on M_{V} alone.

Table 1. The parameters of equation (3) quantifying the dependence on absolute *V*-band magnitude of the effective radius in the SDSS and DES. The Koposov et al. (2008) parameters are taken from fits by Walsh et al. (2009).

Survey	Algorithm	a^*	b^*
SDSS	Koposov et al. (2008, K08)	0.205	1.72
	Walsh et al. (2009, W09)	0.187	1.58
DES	Jethwa et al. (2016, J16)	0.228	1.45

The detection efficiency, ϵ, at fixed M_V, is a function of the radial distance and shows a rapid transition with radius from a 100 per cent to a 0 per cent chance of detection. We may therefore define an equivalent effective detection volume such that, on average, this effective volume includes the same number of satellites of magnitude M_V as predicted by equation (1). The effective radius, $R_{eff}(M_V)$, corresponding to this effective detection volume, is computed by solving the equation,

$$\frac{dN_{sat}}{dM_V} = \int_0^{R_{eff}(M_V)} \Omega r^2 \, dr \, \frac{d^2 N_{sat}}{dr \, dM_V}, \qquad (2)$$

where the left-hand term is given by equation (1) and R_{eff} appears as the upper limit of the integral. The value of R_{eff} depends on both the radial dependence of ϵ and the radial distribution of satellites. As long as the radial distribution of satellites is nearly constant in the interval where the detection efficiency drops from 100 to 0 per cent, R_{eff} can be approximated as the radius at which the detection efficiency is 50 per cent, which is the value that we use in the rest of this paper. This approximation is reasonable as ϵ decreases from 1 to 0 over a narrow radial range (e.g. see fig. 15 in Walsh et al. 2009). Making another choice for the effective radius, such as $\epsilon = 0.9$ (as used in Hargis et al. 2014), would underestimate the effective volume and thus overestimate the inferred satellite count. Both Koposov et al. (2008) and Walsh et al. (2009) show that, to good approximation, the effective detection radius, which corresponds to $\epsilon = 0.5$, is given by

$$R_{eff}(M_V) = 10^{(-a^* M_V - b^*)} \text{ Mpc}, \qquad (3)$$

where a^* and b^* are fitting parameters associated with the search algorithm response function. These values are provided in Table 1 for different algorithms.

The dependence of the effective radius on absolute *V*-band magnitude for the SDSS and DES surveys is shown in the upper panel of Fig. 1. For clarity, in the case of the SDSS we show only the Walsh et al. (2009) response function. For DES we give the Jethwa, Erkal & Belokurov (2016) response function that was shown to give a good match to the actual detections. This is equal to the Koposov et al. (2008) response function as fitted by T08, but shifted to account for the additional depth of the DES compared to SDSS; however, this response function has not been verified at the same level of in-depth analysis as in e.g. Walsh et al. (2009). The figure shows that for the same absolute magnitude, DES is deeper and thus can detect satellites out to greater distances than SDSS. All bright dwarfs, i.e. $M_V < -5.5$ for SDSS and $M_V < -4.0$ for DES, that are within the survey footprint and within our fiducial choice of outer radius, $R_{out} = 300$ kpc, should have been detected within their respective surveys. Thus, the surveys may be considered 'complete' – for the purposes of this analysis – at the absolute magnitudes at which R_{eff} is greater than 300 kpc. Fainter objects can be detected only if they are closer than 300 kpc from the observer, with the faintest,
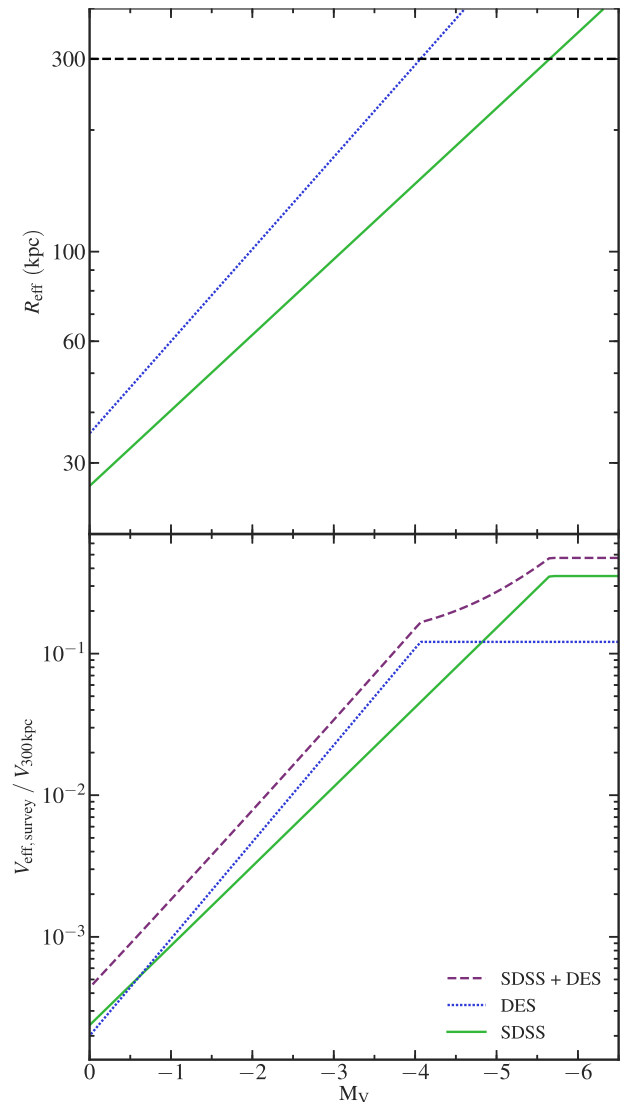

Figure 1. *Upper panel:* the effective detection radius, R_{eff}, of satellites as a function of absolute magnitude, M_V, for the SDSS and DES. The horizontal dashed line indicates our fiducial choice of outer radius, $R_{out} = 300$ kpc, for the MW satellite population. *Bottom panel:* the ratio of the effective volume surveyed by the SDSS and DES, as a function of M_V, to the volume enclosed within 300 kpc. The dashed line shows the combined SDSS plus DES effective volumes. The two panels show the response functions of the W09 and J16 search algorithms, which are given in Table 1.

$M_V = 0$, dwarfs being detected only if they are within ∼30 kpc of the Sun.

To obtain a more informative perspective on the survey completeness, the bottom panel of Fig. 1 shows the ratio between the effective volume of each survey and the total volume enclosed within our fiducial radius of 300 kpc. Even when combining the SDSS and DES footprints, the observations cover only ∼10 per cent of the fiducial volume at $M_V = -4$ and less than 0.1 per cent of the same volume at $M_V = 0$.

3 METHODOLOGY

We require two key ingredients to estimate the total population of satellite galaxies from a given survey of the MW. First, we need

Table 2. The DM particle mass, m_p, softening length, ϵ, and host halo mass, M_{200}, of the AQUARIUS simulations used in this work. Here, M_{200} denotes the mass inside the radius, R_{200}, within which the mean density equals 200 times the critical density.

Simulation	m_p ($M_\odot$)	ϵ (pc)	M_{200} ($10^{12}\,M_\odot$)
Aq-A1	1.712×10^3	20.5	1.839
Aq-A2	1.370×10^4	65.8	1.842
Aq-B2	6.447×10^3	65.8	0.819
Aq-C2	1.399×10^4	65.8	1.774
Aq-D2	1.397×10^4	65.8	1.774
Aq-E2	9.593×10^3	65.8	1.185

a prior for the radial distribution of satellites. For this we take the radial number density of subhaloes in simulations of MW analogues from the AQUARIUS project, which, when subhaloes are selected by v_{peak} – the highest maximum circular velocity achieved in the subhalo's history – is the same as the radial distribution of luminous satellites in hydrodynamic simulations and that of observed MW satellites (see Section 3.1). Secondly, we introduce and test our Bayesian framework used to infer the total number of satellites (Section 3.2). The need for a new methodology is motivated by several shortcomings of previous approaches, which we discuss in detail in Section 3.3.

We assume that the classical satellites, i.e. those with $M_V \leq -8.8$, are bright enough to have been observed by pre-SDSS surveys and that the observations are complete at these magnitudes (therefore ignoring the possible existence of obscured satellites in the Zone of Avoidance). As such, the inferred luminosity function at the bright end will always match the observations, in line with previous studies (e.g. Tollerud et al. 2008). The inference method is only applied to fainter satellites, that is, those with $M_V > -8.8$.

3.1 Tracer population

Any estimation of the total satellite count from incomplete observations needs a prior for the radial number density of these objects, which we estimate from N-body simulations. An ideal simulation from which to extract a tracer population should have high enough resolution for the density profile to be well sampled, and should also offer access to multiple realizations of MW-like haloes to account for host-to-host variations.

The AQUARIUS suite of simulations (Springel et al. 2008) achieves this. It consists of a set of six ΛCDM DM-only N-body simulations of isolated MW-like haloes which were run using the P-GADGET3 code and were labelled Aq-A to Aq-F. In this work we use the 'level 2' simulations (L2, with a particle mass of $\sim 10^4\,M_\odot$), which corresponds to the highest resolution level available across all of the AQUARIUS haloes. Details of these simulations are provided in Table 2. The Aq-F halo experienced a late-time merger, making it unsuitable as representative of the MW halo; consequently, it is not used in this analysis. The cosmological parameters assumed for these simulations are derived from the WMAP first-year data release (Spergel et al. 2003): $H_0 = 73$ km s^{-1} Mpc^{-1}, $\Omega_M = 0.25$, $\Omega_\Lambda = 0.75$, $n_s = 1.0$, $\sigma_8 = 0.9$.

Identifying subhaloes near the centre of simulated haloes using configuration space halo finders like SUBFIND can be difficult (Springel et al. 2008; Onions et al. 2012). Subhalo finders are affected by the resolution of the simulation to which they are applied; these effects can be assessed by comparing haloes which have been simulated at different resolution levels. One of the haloes in the AQUARIUS suite (Aq-A) was simulated at extremely high resolution

('Level 1' or L1, with particle mass of $\sim 10^3\,M_\odot$). Even though the resolution of L2 is still very high, the abundance of subhaloes that are relevant to our analysis is suppressed relative to that at L1, particularly in the inner regions of the halo. The difference between the two levels is comparable to that seen across all other L2 profiles. We can, however, correct for these resolution effects in a relatively straightforward manner, by using the Durham semi-analytic model GALFORM (Lacey et al. 2016; Simha & Cole 2017) to populate the haloes and subhaloes in the AQUARIUS simulations with galaxies and track their orbital evolution even after its halo is no longer resolved (the so-called 'orphan' galaxies). The detailed scheme we used and a comparison of the subhalo samples, both before and after application of GALFORM, are given in Appendix B.

A further factor that needs to be taken into account is the possible destruction of satellite galaxies by tidal interactions with the central galaxy in the halo. This effect has been calculated by Sawala et al. (2017, fig. 4, upper panel) using the APOSTLE hydrodynamic simulations that show that up to 40 per cent of satellites in the inner ~ 30 kpc can be destroyed, although overall the fraction destroyed is much smaller (see also D'Onghia et al. 2010; Errani et al. 2017; Garrison-Kimmel et al. 2017). For our purposes this difference, which changes the radial subhalo distribution, is fairly important but it has the opposite effect to the omission of orphan galaxies and, as we discuss below, the two effects partially cancel out. To correct for these baryonic effects, we downsample the $z = 0$ AQUARIUS subhaloes according to the value of the radius-dependent depletion rate derived by Sawala et al. (2017).[2] The radial dependence of the depletion factor and further details about this procedure are given in Appendix C. We refer to this final population, which incorporates 'orphan galaxies' and baryonic effects, as our fiducial tracer population. Unless otherwise stated, we use this subhalo population throughout the rest of this paper.

We apply a selection cut to the fiducial AQUARIUS subhalo populations on the basis of their v_{peak} values, under the expectation that this will provide a stronger correlation with the likelihood of a galaxy forming within the subhalo (Sawala et al. 2016a) than, for example, selecting by present-day maximum circular velocity or present-day mass (Libeskind et al. 2005; Wang, Frenk & Cooper 2013). This correlation has been shown to hold in the ΛCDM model, which is one of the priors in our analysis. In Fig. 2 we show the radial number density of subhaloes normalized by the mean subhalo density within R_{200}. This is used to assess the appropriateness of applying a v_{peak} selection, and to determine the v_{peak} value down to which the profiles are consistent. We compare this against the radial distribution of luminous satellites selected from a set of high-resolution hydrodynamic simulations from the APOSTLE project (Fattahi et al. 2016; Sawala et al. 2016b). This is a suite of 12 cosmological zoom resimulations of Local Group-like regions run with the P-GADGET3 code and EAGLE subgrid physics models (Crain et al. 2015; Schaye et al. 2015). Of these, four regions – which contain eight MW and M31 analogues – were re-run at much higher resolution and are used here. The APOSTLE data are not used beyond the provision of this reference profile as the simulation is unable to resolve ultrafaint luminous satellites at the magnitudes we are considering here.

Fig. 2 shows that the radial profile of subhaloes is largely independent of the value of v_{peak}, except for values below 10 km s^{-1}, where resolution effects come into play. Most importantly, we find that the

---

[2]There is an error in the values of the fitting parameters quoted by Sawala et al. (2017); see Appendix C for further details and the correct values of the parameters.
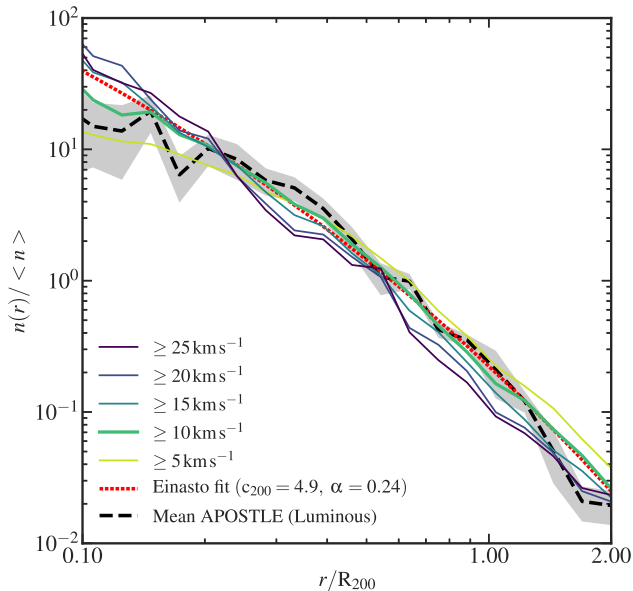
Figure 2. The radial number density of fiducial subhaloes normalized to the mean density within R_{200}. The thin solid lines show the distributions for subhaloes with different v_{peak} cuts averaged over the five AQUARIUS haloes. The thick dashed line and associated shaded region show the radial distribution of *luminous* satellites and its associated 68 per cent scatter obtained using eight haloes from the APOSTLE high-resolution hydrodynamic simulations. The thick dotted line shows the best-fitting Einasto profile. For ease of comparison the profile with our chosen selection criterion of $v_{peak} \geq 10\,\text{km}\,\text{s}^{-1}$ is provided as a thick solid line.

profiles of samples selected with thresholds above this value are in good agreement with the profile of the luminous APOSTLE satellites, and that of observed MW satellites (see Section 3.1.2), making this a good choice to model the radial distribution of satellites. We therefore only consider subhaloes with $v_{peak} \geq 10\,\text{km}\,\text{s}^{-1}$ in the rest of our analysis.

3.1.1 Rescaling the AQUARIUS haloes to a fiducial MW halo mass

We would like to assess if the calculation of the total satellite count is sensitive to the mass of the MW halo. This is important in view of the large uncertainties in current estimates of the MW halo mass, with values typically in the range $(0.5–2.0)\times10^{12}\,\text{M}_\odot$ (e.g. Cautun et al. 2014b; Piffl et al. 2014; Wang et al. 2015). To do this, we rescale the AQUARIUS haloes to a fiducial MW halo mass, $M_{MW, target}$, and apply our Bayesian method to these rescaled haloes. When expressed as a function of rescaled radial distances, r / R_{200}, the radial number density of subhaloes is largely independent of host mass (Springel et al. 2008; Han et al. 2016; Hellwing et al. 2016). Thus, we can rescale the original AQUARIUS haloes to different target masses by multiplying the radial distance of each subhalo by the ratio $R_{200, target} / R_{200, original}$. Unless specified otherwise, the results presented in this paper are calculated for a fiducial MW halo mass, $M_{MW} = 1.0 \times 10^{12}\,\text{M}_\odot$. The variation of these results with MW halo mass is analysed in Section 4.4.

3.1.2 Comparison to the MW satellite distribution

A further test of the appropriateness of a particular choice of tracer population can be obtained by comparing its radial distribution with that of the observed MW satellites. When calculating the latter, we
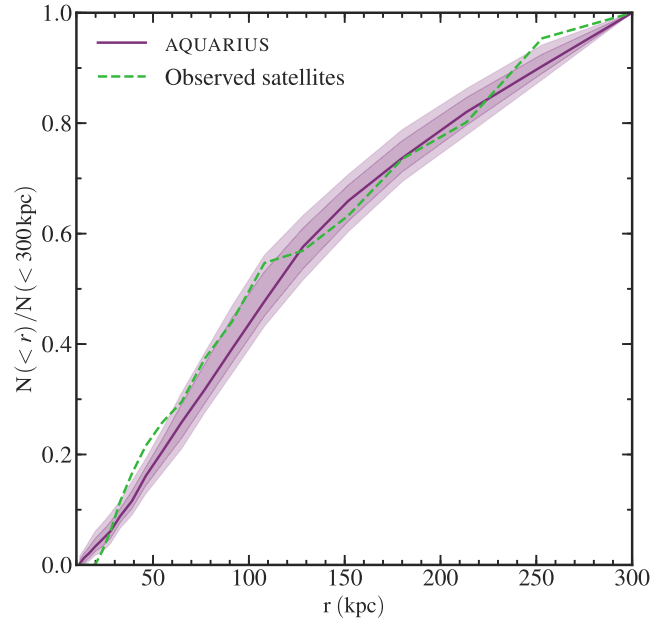

Figure 3. Comparison of the radial distribution of observed MW satellites (dashed line) with that of v_{peak}-selected subhaloes from the five AQUARIUS haloes (solid line) rescaled to a host halo mass of $1.0 \times 10^{12}\,\text{M}_\odot$. The sample of observed satellites was corrected for survey radial incompleteness (see the text) and consists of the classical, SDSS, and DES satellites. We further accounted for the possibility that many of the DES satellites may have fallen in with the LMC by using the probabilities of association with the MW given by Jethwa et al. (2016). The dark and light shaded regions represent the 68 per cent CL and 95 per cent CL (statistical error) bootstrapped error regions for the v_{peak}-selected subhalo distribution, respectively.

need to correct for the radial incompleteness in the surveys: faint satellites can be detected only at small radial distances which, if unaccounted for, leads to a biased, more centrally concentrated satellite distribution. This radial profile, corrected for radial incompleteness, is given by

$$\frac{\text{d}N(r)}{\text{d}r} = \frac{\sum_i P_{MW, i}\, \delta\,(r_i - r)}{\sum_i P_{MW, i}\, \epsilon\,(r, M_{V, i})}, \qquad (4)$$

where the sum is over all the observed classical, SDSS and DES satellites, r_i and $M_{V, i}$ are the position and absolute magnitude of the i-th satellite, and $\delta\,(r_i - r)$ is the Dirac delta function. The quantity, $P_{MW, i}$, denotes the probability that a satellite is associated with the MW, which we take to be 1 for all objects except the DES satellites. Many of these are likely to have fallen in as satellites of the Large Magellanic Cloud (LMC) and, being at first infall, are still concentrated near the position of the LMC which is adjacent to the relatively small region surveyed by the DES. For these objects we use the probabilities of association given by Jethwa et al. (2016); we discuss this point in greater detail in Section 4.1 below. The quantity, ϵ, is the detection efficiency (see Section 2) at distance, r, for satellites of magnitude, M_V, and accounts for radial incompleteness. The denominator of equation (4) is maximal for small r values, where all observed satellites have 100 per cent detection efficiency, and decreases at large r.

Fig. 3 shows that v_{peak}-selected subhaloes have the same radial distribution as the observed MW satellites, as predicted by theoretical arguments (Libeskind et al. 2005). This comparison demonstrates the validity of our fiducial choice for the radial distribution of satellites. The subhalo distribution given in Fig. 3 corresponds to

a MW halo mass of 1.0×10^{12} M$_\odot$ and using a slightly lower value for the MW halo mass leads to an even better agreement between the two radial distributions.

We also used equation (4) to compute the model-independent radial number density for three different observational subsamples: the classical, SDSS, and DES satellites. We find good agreement between the three subsamples (not shown), indicating that the data are consistent with the radial distribution being independent of satellite brightness. This is consistent with Fig. 2, where we find that the radial profile of v_{peak}-selected objects is largely independent of the value of v_{peak}.

3.1.3 A fit to the radial profile of subhaloes

In a later part of our analysis (Section 4.5), we will make use of a functional form for the radial profile of satellites in order to scale our results to different MW halo masses or fiducial volumes. For this, we fit an Einasto profile (Einasto 1965; Navarro et al. 2004)[3] to the $v_{peak} \geq 10$ km s^{-1} curve shown in Fig. 2. The Einasto profile – or the very similar NFW profile (Navarro, Frenk & White 1995, 1996, 1997) – provides a good description of the radial number density of substructures (Sales et al. 2007; Kuhlen et al. 2008; Springel et al. 2008; Han et al. 2016). We can parametrize the Einasto profile in terms of a shape parameter, α, and the concentration, $c_{200} = R_{200} / r_{-2}$, with r_{-2} the scale radius at which the logarithmic slope of the profile is -2. Using the scaled radial distance, $\chi = r / R_{200}$, the Einasto profile is given by

$$\frac{n(\chi)}{\langle n \rangle} = \frac{\alpha c_{200}^3}{3 \left(\frac{\alpha}{2}\right)^{\frac{3}{\alpha}} \gamma \left(\frac{3}{\alpha}, \frac{2}{\alpha} c_{200}^\alpha\right)} \exp\left[-\frac{2}{\alpha} (c_{200}\chi)^\alpha\right], \tag{5}$$

where $\langle n \rangle$ is the mean number density within R_{200} and the lower incomplete Gamma function, γ, is defined as

$$\gamma(s, x) = \int_0^x t^{s-1} \exp(-t) \, dt . \tag{6}$$

We find that an Einasto profile with $c_{200} = 4.9$ and $\alpha = 0.24$ provides a good match to the radial number density of subhaloes, as may be seen in Fig. 2.

3.2 The Bayesian inference method

We are interested in calculating the probability distribution function (PDF) of the total number of satellites, $N_{tot}(< M_V)$, if a survey with effective volume, $V_{eff}(M_V)$, has detected $N_{obs}(< M_V)$ satellites. Note that both the effective volume and the number of satellites are functions of absolute magnitude; however, for ease of readability, we drop the explicit dependence on M_V. Within the Bayesian formalism, the posterior probability of having a total of N_{tot} satellites given that we observe N_{obs} objects within a volume, V_{eff}, is given by

$$P(N_{tot} | N_{obs}, V_{eff}) = \frac{P(N_{obs} | N_{tot}, V_{eff}) P(N_{tot})}{P(N_{obs}, V_{eff})}, \tag{7}$$

where $P(N_{obs}|N_{tot}, V_{eff})$ is the likelihood of having N_{obs} objects within volume V_{eff} if there is a total of N_{tot} satellites. For the prior,

---

[3]A fit to the DM density profile of this form was first introduced in Navarro et al. (2004) but only referred to as the 'Einasto profile' in Merritt et al. (2006).

$P(N_{tot})$, we take a flat distribution; the denominator is a normalization factor. Thus, we have

$$P(N_{tot} | N_{obs}, V_{eff}) \propto P(N_{obs} | N_{tot}, V_{eff}) . \tag{8}$$

The method needs two more ingredients: (1) a prior for the radial distribution of satellites, which we take as that of AQUARIUS v_{peak}-selected subhaloes, and (2) a sample of observed satellites, which we take as that of the SDSS and DES surveys. Thus, N_{tot} represents the inferred total number of MW satellites given these priors.

In practice, it is computationally prohibitive to evaluate the likelihood function over the full parameter space so we use Approximate Bayesian Computation (ABC). ABC methods approximate the likelihood by selecting model realizations that are consistent with the data. For our study, ABC is an accurate way to estimate the likelihood function because (i) we compare the realizations with the actual data rather than with summary statistics and (ii) our data set consists of a discrete number of satellites and our method selects realizations that exactly reproduce the observations.

The likelihood can be computed using a Monte Carlo method applied to each AQUARIUS halo. We start by selecting the satellite tracer population – i.e. the DM subhaloes – within our fiducial MW halo radius and organizing them into a randomly ordered list. Then, for each observed satellite, we estimate the required number of satellites of equal brightness such that there is only one such object inside the effective survey volume corresponding to that observed dwarf galaxy. Starting with the brightest observed satellite, we pick random numbers, N_{rand}, until we find that only one of the top N_{rand} subhaloes is inside the corresponding effective survey volume. The resulting N_{rand} value corresponds to one possible realization of the total count of objects, $N_{tot}(M_V)$, of brightness equal to that of the observed satellite. We then remove the top N_{rand} subhaloes and repeat the same procedure for the next brightest observed satellite.

We considered ordering the subhalo list according to their v_{peak} values, which is equivalent to ordering them from brightest to faintest, assuming that v_{peak} is a luminosity indicator. This ordering would have the advantage of capturing correlations between the luminosity of spatially close satellites as would happen in the case of group accretion. For example, a massive satellite at first infall is likely to bring with it other luminous galaxies (Wang et al. 2013; Shao et al. 2016). In practice, we find that the effects of any such correlations are insignificant compared to the uncertainties introduced by host-to-host variability.

This Monte Carlo procedure generates one possible realization of the dependence of the total number of satellites on absolute magnitude, $N_{tot}(<M_V)$. To sample the full allowed space, the procedure must be repeated many times, for different locations of the survey volume, for different host haloes, and for new randomizations of the subhalo list. The details of how we achieve this are given in Section 3.2.1, together with a more computationally efficient implementation of the Monte Carlo algorithm just described.

Our Monte Carlo approach represents a discrete sampling of the effective volume, V_{eff}, which is a smooth function of M_V. While in principle this may lead to biases, in practice there are enough observed satellites to sample densely the range of absolute magnitudes of interest; thus, any such effects are small, as may be seen in Section 3.2.2.

3.2.1 Practical implementation

For each AQUARIUS halo, we position an observer 8 kpc from the halo centre at one of six vertices of an octahedron, and select a spherical region of 300 kpc in radius centred on this point, similar to Tollerud et al. ([2008](#)). All subhaloes within this region are sorted randomly and assigned an index. We then select a conical region with its apex at the observer position and its opening angle corresponding to the sky coverage of the survey from which the observational data are drawn. The maximum radial extent of the conical region, R_{eff}, for an observed object of given magnitude is calculated using equation (3).

Starting with the brightest object in the survey, of magnitude $M_{V,1}$, we sequentially select subhaloes from our sorted list until we identify one object within our mock survey volume. This sets the lower bound for $N_{tot}(<M_{V,1})$. To set the upper bound, we continue down the sorted list of subhaloes until we find the largest subhalo index which still corresponds to only one subhalo inside the mock survey volume. Every choice between the lower and upper bounds is equally consistent with the observation of one object of $M_{V,1}$ within the survey volume; we therefore randomly select one number in this interval and remove this many subhaloes from the beginning of our ordered list. We then consider the next brightest object – of magnitude $M_{V,2}$ – and repeat the above procedure, using the updated list of subhaloes and the new effective survey volume, $V_{eff}(M_{V,2})$. We continue this process down to the faintest observed satellites in the survey.

The procedure is repeated for 1000 pointings evenly distributed across the simulated sky, and for six observer locations, creating 6000 realizations for each simulated halo. There are five AQUARIUS haloes so, in total, we obtain 3×10^4 realizations that are used to estimate the median and 68 per cent, 95 per cent and 98 per cent uncertainties of the complete satellite luminosity function.

3.2.2 Validation

In order to validate the Bayesian inference method, one of the authors (ON) tested it on a set of 100 mock SDSS observations provided by another (MC). The results of these tests, and a sample of 10 of the mocks, are shown in Fig. 4. The mock observations were generated from a 'blinded' luminosity function – indicated in the figure by the thick dotted line – and were obtained from the Aq-A1 halo distribution of subhaloes with $v_{peak} \geq 10\,\mathrm{km\,s^{-1}}$ within 300 kpc. The selected subhaloes were then randomly assigned absolute magnitudes according to the input luminosity function. Mock observations were produced for 100 random pointings of a conical region analogous to the SDSS volume within the halo, taking into account the effective radius out to which satellites of different magnitudes could be identified. To model better the observations, mocks were generated using a radially dependent detection efficiency: for a given magnitude, using equation (3), we calculated R_{eff}, which is the radius corresponding to a 50 per cent detection efficiency, and then assumed that the detection efficiency decreases from 1 to 0 linearly in the radial range $[0.5, 1.5]\,R_{eff}$. Satellites found in regions where the detection efficiency is below unity were included in the mocks using a probabilistic approach by comparing a random number between 0 and 1 with the value of the detection efficiency. The luminosity functions for a sample of 10 of the 100 resulting mocks are shown as thin solid lines in Fig. 4. Even though all the mocks survey the same halo, we find a large spread in the number of observed satellites.
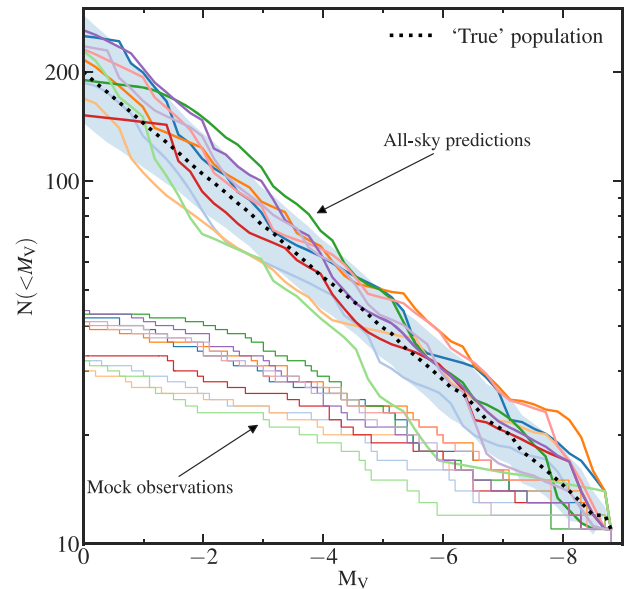

Figure 4. Tests of the Bayesian inference method using mock observations. The thick dotted line shows the input luminosity function used to create 100 SDSS mock observations. The luminosity functions of a sample of 10 of these are shown as thin solid lines. Each of the 10 mock observations was used, in turn, to predict a cumulative satellite luminosity function. The results are shown as thick solid lines. The shaded region represents the 68 per cent uncertainty from one of the mock predictions, shifted to lie on top of the input luminosity function. The dashed lines bound the 68 per cent confidence region over the medians of all 100 mock predictions.

Taking each mock survey data set in turn, we apply the Bayesian inference method, producing 100 estimates of the total satellite luminosity function, 10 of which are shown in Fig. 4 as thick solid lines. To assess the method fully, we also illustrate the 68 per cent uncertainty region, taken from one of the mocks and shifted so that the centre of the region is aligned with the 'true' luminosity function. Most of the inferred satellite luminosity functions lie inside the 68 per cent uncertainty region, in line with statistical expectations, thus demonstrating the success of the method at reproducing the underlying true luminosity function. This uncertainty region, taken from one mock, is comparable to the 68 per cent confidence region obtained from the medians of all 100 mocks, which further demonstrates that the method successfully estimates uncertainties. Note also that our inference method assumes that the detection efficiency is a step function at R_{eff}, but the mocks were generated using a radially varying detection efficiency. Thus, this test also shows that assuming an effective detection radius is a good approximation and does not bias the inferred total luminosity function.

3.3 Comparison to previous inference methods

As we discussed briefly in Section 1, the previous method used for inferring the total satellite count has some drawbacks. The Tollerud et al. ([2008](#), T08) method, which was also employed by Hargis et al. ([2014](#)), used a similar v_{peak}-selected radial distribution of subhaloes as us (although not accounting for unresolved subhaloes or baryonic effects). However, the differences arise from the way in which these distributions are used. The T08 method employs a completeness volume, V_{comp}, that is typically selected as the volume where the detection efficiency, $\epsilon(M_V)$, has a given non-zero threshold value, e.g. $\epsilon(M_V) = 0.9$. Note that the T08 completeness volume
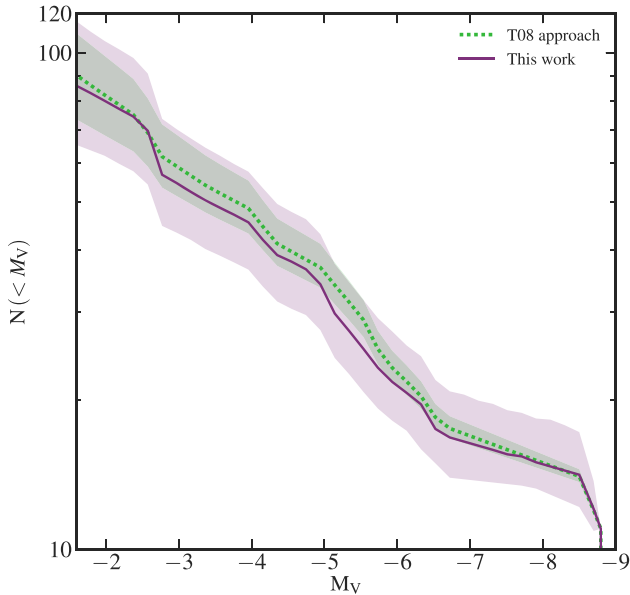
Figure 5. Comparison of two different inference methods for the total dwarf galaxy luminosity function: the Tollerud et al. (2008, T08) method and the Bayesian approach introduced here. Both methods were applied to the same data set, the SDSS. The median estimate (solid line) and associated 68 per cent uncertainties (shaded regions) for each method are shown. The T08 method does not account for stochastic effects, so it underpredicts the uncertainties.

Figure 6. Comparison of the dominant sources of uncertainty in estimates of the total satellite luminosity function: the flattening of the subhalo distribution or the stochastic effects. The region labelled 'fiducial subhalo distribution' corresponds to applying our method to the fiducial subhalo population of the simulated halo, Aq-A1. This estimate is affected by both the shape of the tracer distribution and stochastic effects. The region labelled 'isotropized fiducial distribution' assumes the same radial distribution of subhaloes but with isotropized angular coordinates; this is affected only by stochastic effects. Both approaches have approximately the same median (solid line) and 68 per cent scatter (shaded region). Thus, stochastic effects are a major source of uncertainty.

can be different from the effective volume used in our Bayesian method. To obtain an unbiased estimate, only observed satellites within that completeness volume, i.e. satellites with detection efficiencies above the threshold value, should be used for inferring the total satellite count. The T08 approach is based on calculating, for each observed satellite, the fraction of v_{peak}-selected subhaloes inside the completeness survey volume associated with that satellite. This fraction, $\eta = N_{\text{sub}}\left(< V_{\text{comp}}\right) / N_{\text{max sub}}$, is the ratio of the number of subhaloes, $N_{\text{sub}}\left(V_{\text{comp}}\right)$, inside V_{comp} to the total number of subhaloes, $N_{\text{max sub}}$, inside the halo. Then, for the i-th observed satellite, the fiducial halo volume contains

$$\frac{1}{\eta_i \epsilon_i} \tag{9}$$

satellites of absolute magnitude, $M_{\text{V},i}$, with ϵ_i the detection efficiency associated to the i-th observed satellite.

Fig. 5 shows a comparison of the T08 approach, discussed above, with our Bayesian inference approach. These methods were applied to the same SDSS DR9 data set using the Walsh et al. (2009, W09) completeness function (see Table 1) and the subhalo distribution of a single simulated halo, Aq-A1, corrected for 'orphan galaxies' and baryonic effects. Here, when applying the T08 method, we choose a completeness radius corresponding to $\epsilon(M_{\text{V}}) = 0.5$, which is equal to the effective radius used by the Bayesian method, and only use observed satellites with detection efficiencies, $\epsilon \geq 0.5$. All the satellites detected by the W09 algorithm have $\epsilon > 0.5$ and thus pass this selection criterion. The median estimates produced by the T08 and Bayesian methods are similar. However, as we show in extensive tests detailed in Appendix D, where we apply the T08 approach to mock observations similar to those in Fig. 4, the T08 method underestimates the uncertainties.
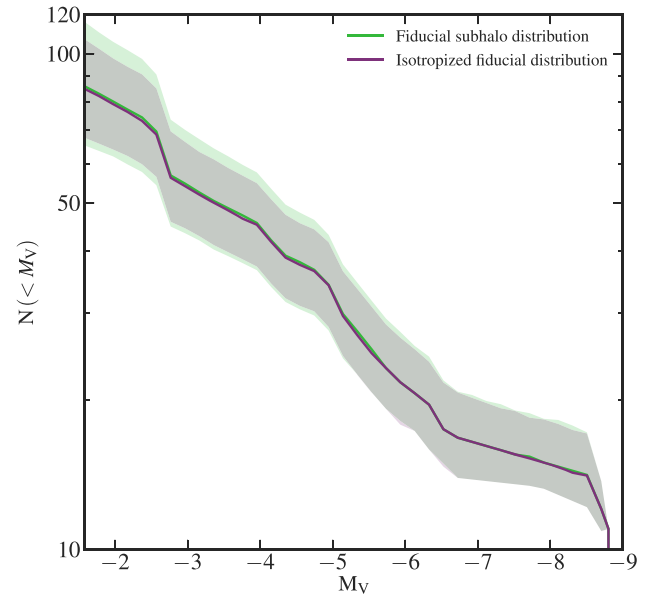
There are two main factors that introduce uncertainties. First, the distribution of satellites is not isotropic but flattened. As a result, surveying different regions of the halo can introduce variations in the number of observed objects. Secondly, the presence or absence of satellites in the observed volume is a stochastic process. Given N satellites and the probability, η, of a satellite being inside the survey volume, then the number of observed satellites in the survey is a binomial distribution with parameters N and η. To determine which of the two effects is dominant, we applied the Bayesian inference method to the original subhalo distribution of the Aq-A1 halo and to many isotropized versions of it. These were generated keeping the same radial distances and isotropizing the angular coordinates. The results of this test, presented in Fig. 6, show that while anisotropy makes a noticeable contribution to the uncertainty at faint magnitudes, stochastic effects are the dominant source of uncertainty.

The T08 method accounts for anisotropy, but it does not account for stochastic effects, which leads to an underestimation of the errors. This underestimate is clearly seen in the mock observation tests detailed in Appendix D, where we find that most of the T08 estimates lie further than the 68 per cent uncertainty interval from the input 'true' luminosity function. Given the probability, η, that a satellite is inside the volume V_{eff}, the T08 method predicts η^{-1} satellites within the halo – see equation (9) without the ϵ term. While this is true on average, for any realization the number of satellites in the halo is given by a negative-binomial distribution with mean value η^{-1}. The width of this distribution, which characterizes the size of the stochastic effects, gives rise to an additional uncertainty that is not included in the T08 methodology.

4 RESULTS

We now provide the results of our analysis using the AQUARIUS haloes rescaled to a fiducial MW halo mass of 1.0×10^{12} M$_\odot$ and within a fiducial radius, $R_{\text{out}} = 300$ kpc. Initially, we perform our analysis for the SDSS and DES data separately, each requiring extrapolations over large unobserved volumes. Combining both surveys reduces the uncertainty because of the larger volume coverage. We also address other issues, for example, the dependence of the inferred total luminosity function on the assumed MW halo mass and on radial distance.

4.1 Separate estimates from SDSS and DES

The results of applying our Bayesian inference method to the SDSS DR9 data set are displayed in the left-hand panel of Fig. 7. Also plotted here is the luminosity function of all satellite galaxies observed in the SDSS DR9 survey for which absolute magnitude measurements have been published to date; these data are provided in Table A1. We adopt the response functions of the two search algorithms detailed in Section 2, by K08 and W09. The counts inferred using the K08 function are systematically higher than those obtained using the W09 function at absolute magnitudes fainter than $M_V \approx -5.5$. This is expected and is a consequence of both algorithms detecting the same number of satellites, but the W09 algorithm probing deeper at fainter magnitudes. The larger scatter in the K08 estimate reflects the additional uncertainty introduced by requiring an extrapolation over larger volumes of the halo. In the remainder of this paper we will use the results obtained using the W09 algorithm as it is able to detect – at least in principle – fainter objects.

Down to magnitude $M_V = -2.7$ (corresponding to the faintest satellite considered by Tollerud et al.), the SDSS data imply that there are at least 64^{+55}_{-26} (98 per cent CL, statistical error – note that the 68 per cent CL is shown in the figure) dwarf galaxies within a radial distance of 300 kpc. This is significantly lower than the estimate by Tollerud et al., who inferred 322^{+144}_{-76} at 98 per cent CL. The Tollerud et al. estimate is higher for two reasons. First, they adopted the K08 response function which is shallower than the W09 function. Secondly, their estimates were based on the SDSS DR5 data release that observed 10 satellites over a footprint of ~8000 square degrees. Since then, while SDSS DR9 has added an additional ~6500 square degrees of sky coverage, it has detected only four new satellites brighter than $M_V = -2.7$.

The result of applying our method to the DES is shown in the right-hand panel of Fig. 7; in this case we adopt the Jethwa et al. (2016) response function. No satellites are detected in DES with magnitude in the range $-8.9 \lesssim M_V \lesssim -4.5$, so we interpolate between the values calculated at each end of the range. Including all the DES satellites in the inference method returns twice as many satellites with $M_V \lesssim -4$ than inferred from the SDSS satellites alone. This discrepancy is caused by the DES footprint being adjacent to the two Magellanic Clouds which, models suggest, are on their first infall (Kallivayalil et al. 2013; Jethwa et al. 2016). If that were the case, then it is likely that the two Magellanic Clouds would have contributed their own complement of satellite galaxies. These are not distributed uniformly over the sky, but are still clustered around the Magellanic Clouds (Sales et al. 2011). As many as half of the satellites detected by DES could have come from the LMC (Sales et al. 2007; Jethwa et al. 2016). Failing to account for these localized associations would lead to an overestimate of the total Galactic satellite population. We adopt the probabilities

of association of each of the DES objects with the LMC inferred by Jethwa et al. (2016) and include an additional step in our analysis: for each mock survey pointing, we generate a Monte Carlo realization in which the DES satellites are assigned either to the MW or to the LMC according to these probabilities. Only the DES satellites assigned to the MW are then included in the Bayesian inference.

The right-hand panel of Fig. 7 shows the satellite luminosity function accounting for the association of some DES satellites to the LMC. This estimate is in good agreement with the estimate from the SDSS for $M_V \lesssim -4$. The discrepancy at brighter magnitudes is due to the lack of detection in the DES of any satellites brighter than $M_V = -4.5$ within a distance of 300 kpc. While DES is deeper than SDSS, it covers a smaller area on the sky and thus, for $M_V \lesssim -5$ and $M_V \gtrsim -0.5$, DES samples a smaller effective volume than SDSS (see Fig. 1). Nonetheless, the luminosity function inferred from DES is generally consistent with that inferred from SDSS, given the large uncertainties in both estimates.

4.2 Combined estimate from SDSS+DES

The best estimate of the total satellite luminosity function is obtained by combining the SDSS and DES. We modify the analysis described in Section 3.2.1 by including a second conical region oriented relative to the first one such that it reproduces the approximate orientation of the real SDSS and DES. The SDSS vector is used to define the pointing 'direction' of this configuration; it uniformly samples the sky as before. The second vector – corresponding to the DES – is fixed at an angle of $120°$ relative to the SDSS vector but is allowed to rotate around it. For each SDSS pointing a configuration is generated and a combined SDSS+DES luminosity function is calculated. In practice, this analysis corresponds to that of a survey of effective volume, $V_{\text{eff, SDSS}} + V_{\text{eff, DES}}$, consisting of two disjoint regions. The analysis otherwise proceeds as before.

The predicted total satellite luminosity function from the combined SDSS+DES data is shown in Fig. 8. This estimate is consistent with those from the separate analyses of SDSS and DES data: except in a few bins, the medians of the individual estimates lie within the 68 per cent uncertainty range of the SDSS+DES estimate. When comparing with the combined result, we find that the SDSS-only estimate overpredicts the satellite count for $M_V \leq -4$, which is to be expected given that DES did not find any satellites brighter than $M_V = -4.5$ within our fiducial radius of 300 kpc. In contrast, for $M_V > -4$, the SDSS-only estimate occasionally lies slightly below the total satellite count, reflecting the large number of satellites with $M_V \geq -4.5$ observed by DES. The data associated with Fig. 8 are provided in Table E1 of Appendix E.

We find that the total satellite luminosity function is well-fitted by the broken power law:

$$\log_{10} N(<M_V) = \begin{cases} 0.095 M_V + 1.85 & \text{for } M_V < -5.9 \\ 0.156 M_V + 2.21 & \text{for } M_V \geq -5.9 \end{cases}, \quad (10)$$

that is, the faint end of the luminosity function is described by a significantly steeper power law than the bright end.

4.3 Dependence on the tracer population

In Section 3.1 we argued that in order to make accurate predictions, it is necessary to incorporate two effects into the analysis: the inclusion of unresolved subhaloes, i.e. 'orphan galaxies', and the depletion of subhaloes due to tidal disruption by the central galaxy disc (i.e. baryonic effects). These changes primarily involve
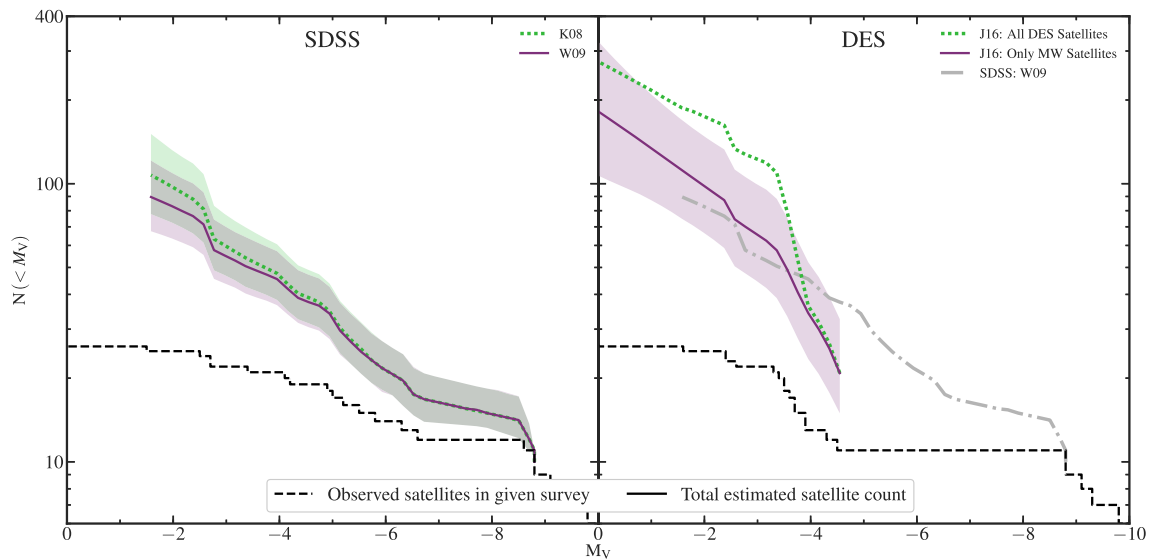
Figure 7. The total MW satellite galaxy luminosity functions inferred from the SDSS and DES (left- and right-hand panels, respectively). The solid lines and corresponding shaded regions show the median estimates and associated 68 per cent uncertainties. The dashed lines indicate the number of observed satellites within 300 kpc in each of the two surveys; these are input into the Bayesian inference method. For the SDSS, we show estimates using the response functions of the two search algorithms devised by Koposov et al. (2008, K08) and Walsh et al. (2009, W09). Both algorithms detect the same number of satellites, but the latter probes down to fainter magnitudes. For DES, we use the Jethwa et al. (2016, J16) response function. This result is truncated at $M_V \leq -4.5$ as no satellites brighter than this have been observed in DES within 300 kpc. The DES estimate (solid line) accounts for the possibility that some objects observed by DES may be satellites of the LMC. For reference, we also plot a second estimate which assumes that all DES objects are associated with the MW (dotted line), as well as the SDSS W09 result (dot–dashed line).
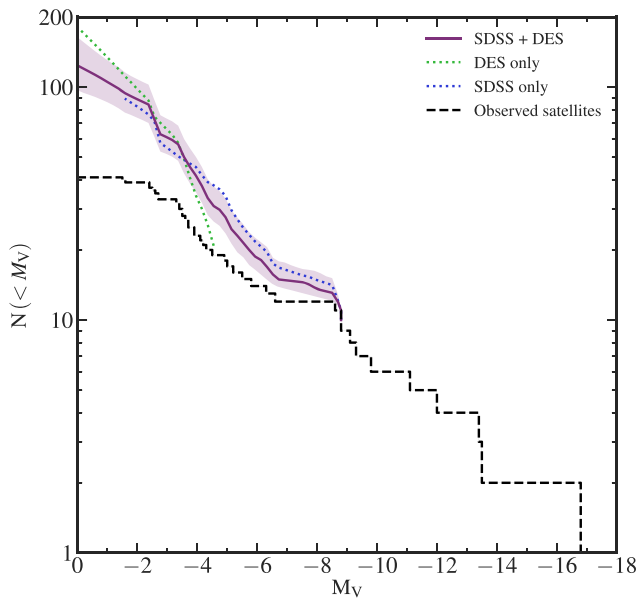

Figure 8. The total luminosity function of dwarf galaxies within a radius of 300 kpc from the Sun obtained from combining the SDSS and DES data. The solid line and the shaded region show the median estimate and its 68 per cent uncertainty, respectively. The two dotted lines show the median satellite luminosity functions using SDSS and DES data separately. The luminosity function of all observed satellites within the SDSS and DES footprints inside 300 kpc is indicated by the dashed line. The total satellite luminosity function is well-fitted by the broken power law given in equation (10).
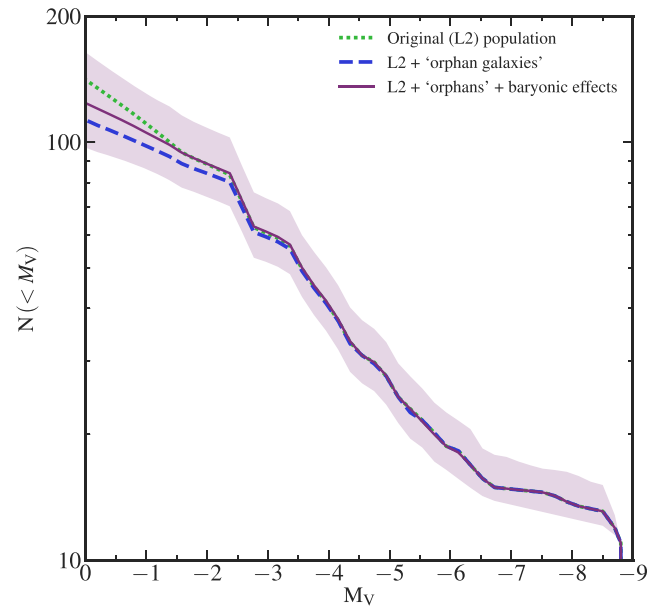

Figure 9. The sensitivity of the inferred satellite luminosity function to the two corrections applied to the subhalo population. The dotted line shows the inferred satellite count using the original subhalo distribution of AQUARIUS. The dashed line shows the effect of adding subhaloes missing due to resolution effects, the so-called 'orphan galaxies'. The solid line shows the results from our analysis, in which we also account for subhalo depletion due to baryonic effects. The shaded region indicates the 68 per cent uncertainty region of our final result.
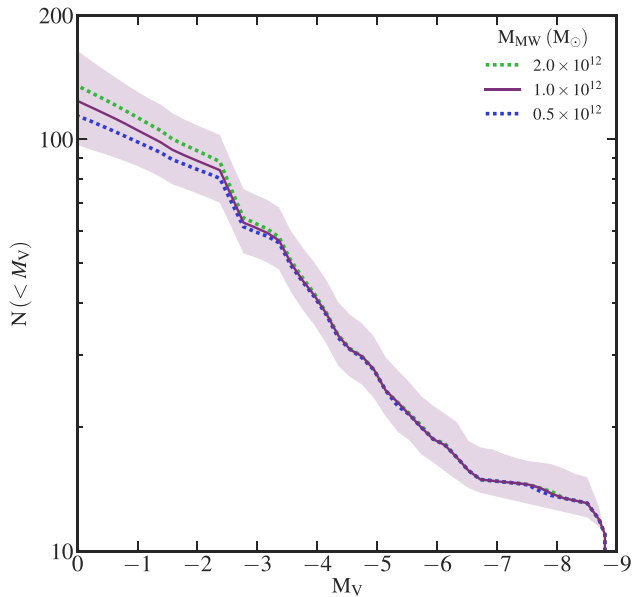
Figure 10. The dependence of the inferred total dwarf galaxy luminosity function within 300 kpc on the assumed mass of the MW halo. The lines show estimates for our fiducial MW halo mass of $1.0 \times 10^{12}\,\mathrm{M_\odot}$ (used in previous plots) and for lighter and heavier MW haloes, as indicated in the legend. For the fiducial case, we show the median estimate (solid line) and the 68 per cent uncertainty (shaded region). For the other two cases we show only the median estimates (dotted lines).

Figure 11. The radial dependence of the total number of satellites enclosed within radius r. The Y-axis gives the ratio of this number relative to the satellite count within 300 kpc, the fiducial radius used in this analysis. The result is independent of absolute magnitude, M_V, since subhaloes with different v_{peak} cuts have the same radial profile. There is little dependence on the mass of the MW halo.

the inner ~50 kpc of the halo, the region to which the faint end of the luminosity function is most sensitive. Although these two effects have opposite sign, they do not cancel out completely. In Fig. 9 we show the effect of each of the two corrections, which are only important for the faintest satellites ($M_V > -2$). Prior to any correction, the $M_V = 0$ satellite count is 141^{+54}_{-35}; the addition of unresolved subhaloes reduces this to 113^{+34}_{-24}. This is because the unresolved subhalo population is very centrally concentrated; on average some ~85 per cent of them lie within 50 kpc. Accounting for subhalo depletion due to baryonic effects produces a small upward shift in the median to 124^{+40}_{-27}; a decrease of ~12 per cent relative to the uncorrected luminosity function inferred using the L2 subhalo distribution of AQUARIUS haloes.

4.4 Dependence on the mass of the MW halo

As we discussed in Section 3.1.1, the MW halo mass is poorly constrained, with recent estimates varying within a factor of 2 from our fiducial choice of $M_{MW} = 1.0 \times 10^{12}\,\mathrm{M_\odot}$ (see the compilation of Wang et al. 2015). To investigate the sensitivity of the inferred total satellite luminosity function to the MW halo mass, we repeated our analysis for two extreme mass values, $0.5 \times 10^{12}\,\mathrm{M_\odot}$ and $2.0 \times 10^{12}\,\mathrm{M_\odot}$, corresponding roughly to lower and upper bounds for the MW halo mass (e.g. Wang et al. 2015). To obtain estimates for these halo masses, we rescaled the fiducial radial distribution of subhaloes using the procedure described in Section 3.1.1. The inferred dwarf galaxy luminosity functions are displayed in Fig. 10, which shows that despite the factor of 4 difference between the lowest and highest halo masses considered, no large discrepancies begin to emerge until $M_V \geq -2.5$. Even at fainter magnitudes, the differences are well within the 68 per cent uncertainty range for a given MW halo mass.
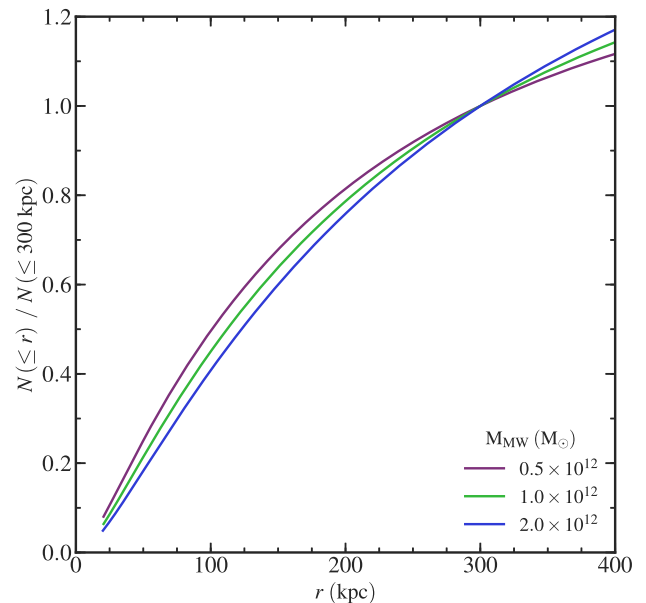
The number of subhaloes in a DM halo scales strongly with halo mass (e.g. Wang et al. 2012; Cautun et al. 2014a), so naively we might assume that the inferred satellite count follows the same relation. As Fig. 10 demonstrates, that is not the case; we see only a weak variation of N_{tot} with M_{halo}. The inferred satellite count depends only on the shape of the normalized radial profile of subhaloes, and not on the *total* number of subhaloes. When expressed in terms of r/R_{200}, i.e. radial distance in units of the virial radius of the halo, the radial profile is largely independent of host mass (Springel et al. 2008; Han et al. 2016; Hellwing et al. 2016). Different host masses correspond to different values of R_{200}, and thus any features in the radial profile are mapped on to different physical radial distances. If the radial distribution of subhaloes were a power law, then the inferred satellite count would be independent of halo mass: for fixed r, changing R_{200} would only lead to a shift in the normalization of the radial profile, which is unimportant for our analysis.

4.5 Dependence on the outer radius cut-off

Fig. 11 illustrates the dependence of the total satellite count within a given radius, r, as a function of r. These estimates follow from the observation that the radial number density of subhaloes selected above a v_{peak} threshold is independent of the value of the threshold (see Fig. 2), which suggests that the radial distribution of satellites should also be independent of satellite luminosity.

The fiducial radial distribution of subhaloes is well described by an Einasto profile: the number of satellites within $\chi = r/R_{200}$ is given by

$$N(<\chi) = 4\pi \int_0^\chi n(\chi')\,\chi'^2\,\mathrm{d}\chi', \qquad (11)$$

with $n(\chi')$ the Einasto profile given by equation (5). Performing the integration and substituting for χ gives

$$N(<r) = N(<300\,\text{kpc}) \frac{\gamma\left(\frac{3}{\alpha}, \frac{2}{\alpha}\left[c_{200}\chi\right]^\alpha\right)}{\gamma\left(\frac{3}{\alpha}, \frac{2}{\alpha}\left[c_{200}\frac{300\,\text{kpc}}{R_{200}}\right]^\alpha\right)}, \quad (12)$$

where the function γ is given by equation (6). The radial dependence of $N(<r)$ is affected by the assumed value for the MW halo mass through the dependence of R_{200} on halo mass. Fig. 11 shows the radial dependence of $N(<r)$ for the three MW halo masses assumed in Fig. 10; we find only a mild variation with MW halo mass. Extending to distances farther than 300 kpc leads only to modest increases in the satellite count, with an ~20 per cent increase at 400 kpc, which is roughly half way between the MW and M31. Of all the satellites within 300 kpc, ~80 per cent of them lie within 200 kpc, the R_{200} value for a $1.0 \times 10^{12}\,M_\odot$ halo mass. At even smaller radial distances, we find ~45 per cent of the satellites within 100 kpc.

4.6 Apparent magnitude luminosity function

In this subsection we examine the prospects for discovery of faint satellites in future surveys of the MW. For simplicity we assume that the only factor that determines the detectability of a satellite is its apparent luminosity, rather than its size or surface brightness. We can then calculate the number counts of satellites as a function of V-band magnitude. To estimate apparent magnitudes, we assign an absolute magnitude, M_V, to subhaloes by sampling the inferred luminosity function from Section 4.2, i.e. the combined SDSS+DES estimate. We then use the subhalo distance from the halo centre to compute the distance modulus and thus the apparent magnitude. This process is repeated for the luminosity functions generated from each pointing and observer location combination – 6000 in all. The results presented in this section are for a MW halo mass of $1.0 \times 10^{12}\,M_\odot$ and for a 300 kpc outer radius.

Dwarf galaxy counts as a function of apparent magnitude are shown in Fig. 12, where we split the population into two classes: ultrafaint and hyperfaint dwarf galaxies, which we define as objects in the absolute magnitude ranges: $-8 < M_V \leq -3$ and $-3 < M_V \leq 0$, respectively. Within 300 kpc from the MW, we expect to find 46^{+12}_{-8} (68 per cent CL, statistical error) ultrafaint and 61^{+37}_{-23} (68 per cent CL, statistical) hyperfaint dwarfs. The first number can be compared to the slightly higher estimate of 66^{+9}_{-7} (68 per cent CL) ultrafaints provided by Hargis et al. (2014), based solely on data from SDSS DR8. We showed in Fig. 8 that this population is usually overestimated in predictions based only on SDSS because of a higher abundance of ultrafaint satellites in the SDSS field than would be expected from the total observed population. As discussed in Section 3.3, their uncertainties are also 28 per cent too small as stochastic effects were not accounted for in their estimate. Most ultrafaints have apparent magnitudes brighter than 18, so surveys just 0.5 magnitudes deeper than DES – which can detect satellites down to $m_V = 17.5$ – should be deep enough to observe most ultrafaint dwarfs in the MW. The luminosity function of hyperfaint dwarfs extends much fainter, with most satellites having $m_V < 21.5$. Discovering these would require a survey 4 mag deeper than DES; Large Synoptic Survey Telescope (LSST) is one such future survey. An all-sky DES-like survey would only lead to the detection of ~30 hyperfaint dwarfs, a factor of 4 more than the currently known population.
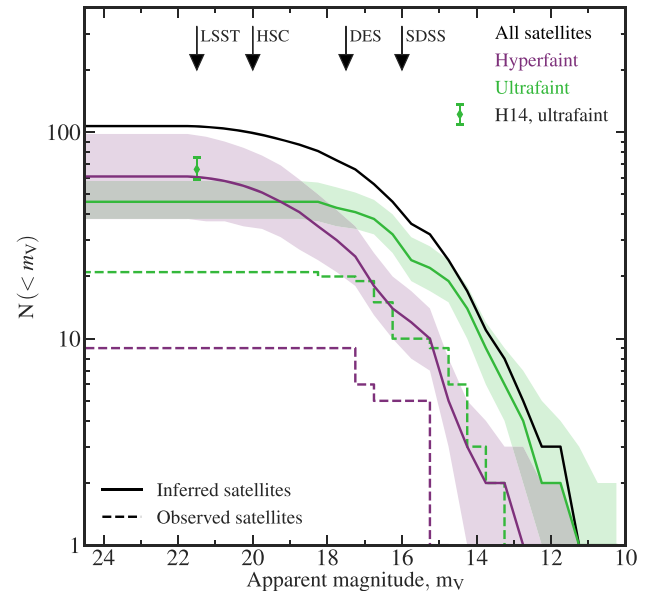

Figure 12. The inferred Galactic satellite number counts within 300 kpc as a function of apparent V-band magnitude, m_V. The satellites are split into ultra- and hyperfaint dwarf galaxies, which correspond to objects with absolute magnitude in the range $-8 < M_V \leq -3$ and $-3 < M_V \leq 0$, respectively. The solid lines display the median prediction, with the corresponding shaded regions indicating the 68 per cent uncertainties. For reference the sum of the median predictions of both populations is also provided (black line). The diamond and associated error bars represent the Hargis et al. (2014, H14) prediction and 68 per cent uncertainty region for the total expected number of ultrafaint satellites. As before, the dashed lines display number counts of observed ultra- and hyperfaint dwarf galaxies within the SDSS and DES. The vertical arrows indicate the faintest satellites that can be detected in past and future surveys: SDSS ($m_V = 16.0$), DES ($m_V = 17.5$), HSC ($m_V = 20.0$), and LSST ($m_V = 21.5$).

5 DISCUSSION

We have made new predictions for the total MW satellite luminosity function by extrapolating the numbers of satellites currently known using a new Bayesian inference method. As input data we use a combination of the recently discovered satellites in the DES and the population previously known from SDSS DR9. As a prior for the radial distribution of the MW satellites, which is needed for the extrapolation, we use the radial distribution of subhaloes in the AQUARIUS simulations of galactic haloes having peak maximum circular velocity, v_{peak}, above a given threshold. We correct the subhalo distribution for unresolved subhaloes and account for subhalo depletion due to tidal disruption by the central disc. We showed in Fig. 3 that the radial distribution of v_{peak}-selected subhaloes provides a good match to that of the observed MW satellites. We improve upon previous studies by introducing a new Bayesian inference method, which overcomes the limitations of earlier approaches. We also explore the effect of uncertainties in the MW halo mass and derive a relation for rescaling our estimates to different radii.

We find that, for a $1.0 \times 10^{12}\,M_\odot$ MW halo, there are 124^{+40}_{-27} (68 per cent CL, statistical error) satellites brighter than $M_V = 0$ within 300 kpc of the Sun, which is slightly inconsistent with the result from Hargis et al. (2014). Our estimate is consistent with that of Jethwa et al. (2016) when adjusted for differing outer radii; their estimate lies at the upper end of our 68 per cent uncertainty range. Our lower estimate is due to the inclusion of orphan galaxies and baryonic effects, which decrease the inferred count of MW satellites (see Fig. 9). Compared with the Tollerud et al. (2008) estimate of

322^{+144}_{-76} (98 per cent CL) satellites brighter than $M_V = -2.7$ within 300 kpc, our estimate of 66^{+39}_{-20} (98 per cent CL, statistical) is a factor of ~5 lower. The origin of this discrepancy is primarily the use by Tollerud et al. of the shallower K08 response function as opposed to the W09 function that we use here. Furthermore, since their work, the SDSS footprint has increased in size by ~80 per cent, while the number of discovered satellites inside this footprint has increased by very little. We also note that previous studies have underestimated their uncertainty ranges because they have not properly accounted for stochastic effects, which are broadly independent of satellite brightness (see Section 3.3 for a more in-depth discussion).

The future detection of dwarfs depends on their apparent magnitude and we can estimate the luminosity thresholds that future surveys will need to exceed in order to detect the satellite population inferred in this study. In our total inferred population there are 46^{+12}_{-8} (68 per cent CL, statistical) ultrafaint dwarf galaxies (with magnitudes in the range $-8 < M_V \leq -3$), of which ~20 have been observed so far. We find that the majority of these have apparent magnitudes brighter than $m_V = 18$; these would be discoverable with surveys just 0.5 magnitudes deeper than DES. There are ~30 such dwarfs still to be discovered in the MW, of which ~7 should lie inside the SDSS DR9 footprint but beyond its detection limit. Our 61^{+37}_{-23} (68 per cent CL, statistical) hyperfaint dwarfs (with magnitudes $M_V \geq -3$) make up some 62 per cent of our total population and have apparent magnitudes brighter than $m_V = 21$; discovering these would require a survey 4 mag deeper than DES. The planned LSST survey should cover approximately half of the sky and will therefore be able to find half of the inferred count of 61^{+37}_{-23} hyperfaint dwarfs. The sizes of both populations are slightly inconsistent with the lower end of estimates by Hargis et al. (2014).

Our inferred satellite galaxy luminosity function likely represents a lower limit to the true population. Our method takes the observed satellites, which are found in surveys with various detectability limits, as a sample of the global population. In particular, the observed surface brightness cut-off suggests that there could be a population of faint, spatially extended dwarfs that are inaccessible to current surveys (e.g. see Torrealba et al. 2016a). To account for this in our method would require deeper observations than are currently available.

A further complication arises from the presence of the LMC, which, given its large mass, is likely to have brought its own complement of satellites. The LMC may be on its first infall (Sales et al. 2011; Kallivayalil et al. 2013; Jethwa et al. 2016) and the spatial distribution of the satellites it brought with it could be very anisotropic (Jethwa et al. 2016). While we accounted for the probability that a large fraction of DES detections may be associated with the LMC, our analysis does not account for the presence of LMC satellites outside the DES footprint. To do so would require a prior on the present-day spatial distribution of LMC satellites. Before infall, the LMC could have had perhaps as much as a third of the MW satellite count (Jethwa et al. 2016), though this estimate is very uncertain due to poor constraints on the MW and especially the LMC halo mass. At face value, this could add at most ~50 satellites to the total count.

Inherent to all analyses that estimate the satellite luminosity function are several systematics which, with a few exceptions, mainly affect the faint end of the luminosity function. The most important of these is the assumed radial distribution of subhaloes, which needs to be determined from cosmological simulations. We showed that the distribution of v_{peak}-selected subhaloes matches both the luminosity-independent radial distribution of observed MW satellites and that of state-of-the-art hydrodynamic simulations such as APOSTLE (see Figs 2 and 3); consequently, we think that any system-

atic effect on the inferred satellite count arising from our choice of fiducial tracer population is likely to be small. To obtain our fiducial subhalo sample, we needed to correct for two effects that are not well understood. Even the highest resolution simulations, such as those of the AQUARIUS project, can suffer from resolution effects, particularly near the centre of the host halo. This issue is common to *all* cosmological simulations, and we addressed it by including 'orphan galaxies' (i.e. galaxies whose haloes have been disrupted) identified by applying the Durham semi-analytic model of galaxy formation, GALFORM, to the AQUARIUS simulations. This effect is only significant for the faint end of the satellite luminosity function ($M_V \gtrsim -3$) since ~85 per cent of the orphan population lies within 50 kpc of the centre, the region to which the faint end is most sensitive. We also accounted for baryonic effects on the subhalo mass function by lowering its amplitude in accordance with the prescription in Appendix C, using depletion factors based on the APOSTLE project (Sawala et al. 2017). Garrison-Kimmel et al. (2017) argued for a larger depletion in the inner ~30 kpc than Sawala et al., while Errani et al. (2017) claim that, due to their limited resolution, most simulations overpredict the subhalo depletion factor. As discussed in Section 4.3, although this correction introduces noticeable changes in the predicted satellite luminosity function, these lie within our error bounds, and are smaller in magnitude than those introduced by the addition of orphan galaxies. These changes primarily affect the faint end of the satellite luminosity function above $M_V \geq -2$, which is also the most theoretically and observationally uncertain part of the luminosity function independently of these effects.

A second important systematic is the choice of observed satellite population. In this work we used satellites discovered in the SDSS and DES. Although all satellites in the former have been spectroscopically confirmed as DM-dominated dwarf galaxies, over three-quarters of the DES satellites have not (yet). We choose to use *all* DES satellites in our analysis. This is motivated by considering the size–magnitude plane (e.g. Drlica-Wagner et al. 2015, fig. 4) that shows that most DES satellites are more consistent with the properties of Local Group galaxies than with the population of known globular clusters. Reclassifying some of the DES detections as globular clusters would lower the inferred total satellite count at the faint end of the luminosity function ($M_V \geq -4$), but would not affect the bright end. Given the good agreement between the SDSS-only and DES-only estimates of the total satellite count, we predict that most DES detections are dwarf galaxies.

The mass of the MW halo is poorly constrained. However, the inferred satellite luminosity function is largely independent of the host halo mass, except at magnitudes fainter than $M_V = -3$ where it shows a very weak mass dependence (see Fig. 10). Instead of marginalizing over the MW halo mass distribution, we provide a means of converting between halo masses at the extremes of the range of constraints.

The MW is the smaller partner of a paired system, which could introduce anisotropies into the MW's substructure due to interactions with M31; these would be manifest in the form of more correlated structure. Our choice of 300 kpc for our fiducial radius is less than the midpoint of the MW-M31 distance, minimizing any effects from interactions with M31 and allowing us to model the MW approximately as an isolated halo. In addition, this value is often used in the literature (e.g. Hargis et al. 2014; Jethwa et al. 2016) and is close to the expected virial radius of the MW halo. Our choice of fiducial radius should not be interpreted as precluding the eventual discovery of other satellites further out than this.

The dependence of the total satellite count on MW halo mass is not determined by the number of subhaloes at fixed mass, but by the

shape of the normalized subhalo radial number density profile. A weak halo mass dependence arises from the non-power-law nature of the subhalo radial profile: features in this profile are remapped to different physical distances for different halo masses, resulting in a variation in the predicted luminosity function. As a direct consequence, this implies that changes in the assumed MW halo mass, which determines the number of DM substructures, alter the abundance matching relation for Galactic dwarfs; in this regime not all subhaloes of a given mass host a visible galaxy (Sawala et al. 2015). We find that doubling the halo mass roughly doubles the number of subhaloes (Wang et al. 2012; Cautun et al. 2014a), so that there are more of them at fixed $v_{\rm peak}$. A more massive MW halo would then require the same dwarfs to be placed in subhaloes with higher $v_{\rm peak}$ than they would for a lower MW mass halo.

The spatial distribution of subhaloes – upon which our predictions rely – is partly determined by cosmology but is also affected by the internal dynamics of haloes. In turn, these are influenced by the mass function of subhaloes and their accretion rate, both of which are fairly universal in both ΛCDM and WDM models (Springel et al. 2008; Ludlow et al. 2016). Recent work by Bose et al. (2017) has shown that the radial distribution of subhaloes is broadly independent of the nature of the DM. Our predictions are therefore applicable to other DM models and can, in fact, be used to constrain the masses of WDM particles.

6 CONCLUSIONS

An estimate of the MW's complement of satellite galaxies is required until deeper, more complete surveys that could discover more faint galaxies are undertaken in the next few years. These predictions can be used to address numerous outstanding astrophysical questions, from understanding the effects of reionization on low mass haloes, to constraining the properties of DM particles.

In this work we have, for the first time, combined data from SDSS and DES – which together cover nearly half of the sky – to infer the MW's full complement of satellite galaxies. Our method requires a prior for the radial distribution of satellites, which we obtain from the subhalo populations of the AQUARIUS suite of high-resolution DM-only simulations in which we account for the competing effects of resolution and subhalo depletion due to interaction with the central baryonic disc (see Section 5). We have shown that selecting subhaloes by their peak maximum circular velocity provides a good match to the radial distribution of observed MW satellites (see Fig. 3).

The Bayesian method we have introduced to make these estimates overcomes some of the limitations of previous analyses (see Fig. 5), and properly accounts for stochastic effects. For each observed dwarf galaxy, the method estimates how many objects are needed to find one such satellite in the survey volume. These results are averaged over multiple DM haloes to characterize uncertainties arising from halo-to-halo variation.

Within 300 kpc of the Sun – and assuming a MW halo mass of $1.0 \times 10^{12}\,{\rm M}_\odot$ – we predict that the MW has 124^{+40}_{-27} (68 per cent CL, statistical error) satellites brighter than $M_{\rm V} = 0$ (see Fig. 8). Of these, we expect to find 46^{+12}_{-8} (68 per cent CL, statistical) ultrafaint dwarf galaxies ($-8 < M_{\rm V} \le -3$), a result that is marginally inconsistent with the lower end of the Hargis et al. (2014) estimate, but nearly a factor of 5 smaller than the Tollerud et al. (2008) estimate. All the Galactic ultrafaints could be detected by a survey just 0.5 magnitudes deeper than DES. We also expect to find a population of 61^{+37}_{-23} (68 per cent CL, statistical) hyperfaint dwarfs ($-3 < M_{\rm V} \le 0$), and to obtain a full census of this population would need a survey 4 mag deeper than DES. The LSST survey should be

able to see at least half of this faint population of dwarf galaxies in the next decade.

In all methods seeking to estimate the total luminosity function, certain assumptions must be made. In particular, an important assumption is the radial distribution of the true satellite population, which is best inferred from a cosmological simulation. Here, we have used a set of the highest resolution DM-only simulations available and, most importantly, a method for selecting the subhaloes that are expected to host satellites that has been shown to give consistent results for a number of observed properties of the MW satellite population, such as the radial distribution of and counts of bright observed MW satellites. This does not guarantee that the extrapolation is free of systematic effects but as Fig. 3 shows, in the regime where we can check with available data, any such systematics are small.

The estimates above represent only lower limits to the total number of Galactic satellites (see Section 5) because they do not take into account very low surface brightness objects that may have been missed in current observations. In addition, the estimate does not account for some of the satellites brought in by the LMC which today lie outside the DES footprint (which at most would increase the total count by 30 per cent).

While our key results assume a MW halo mass of $1.0 \times 10^{12}\,{\rm M}_\odot$, our analysis shows that the predicted dwarf galaxy luminosity function is independent of host halo mass for objects brighter than $M_{\rm V} = -3$ (see Fig. 10). For fainter satellites we find a weak dependence on halo mass, with a more massive MW halo playing host to more satellites. Our tests assuming extreme MW halo mass values ($[0.5, 2.0] \times 10^{12}\,{\rm M}_\odot$) reveal that the resulting luminosity functions lie well within the 68 per cent uncertainty range calculated for our fiducial MW halo mass. Of the dwarfs within our fiducial distance of 300 kpc, ∼45 per cent and ∼80 per cent are found within 100 and 200 kpc, respectively.

The results of this study provide a useful reference point for comparing theoretical predictions with the measured abundance of satellite galaxies in the MW. However, it must be borne in mind that the MW is only one system and that the abundance of satellites around similar galaxies exhibits considerable scatter (Guo et al. 2012; Wang & White 2012).

The code that implements our method to estimate the total population of MW satellite galaxies is available online (Newton & Cautun 2018). In addition, we also make available all data that are required to reproduce our results (e.g. Fig. 8).

REFERENCES

Adelman-McCarthy J. K. et al., 2007, ApJS, 172, 634

Alam S. et al., 2015, ApJS, 219, 12

Avila-Reese V., Colín P., Valenzuela O., D'Onghia E., Firmani C., 2001, ApJ, 559, 516

Bechtol K. et al., 2015, ApJ, 807, 50

Benson A. J., Lacey C. G., Baugh C. M., Cole S., Frenk C. S., 2002a, MNRAS, 333, 156

Benson A. J., Frenk C. S., Lacey C. G., Baugh C. M., Cole S., 2002b, MNRAS, 333, 177

Bode P., Ostriker J. P., Turok N., 2001, ApJ, 556, 93

Bose S. et al., 2017, MNRAS, 464, 4520

Bullock J. S., Kravtsov A. V., Weinberg D. H., 2000, ApJ, 539, 517

Bœhm C., Schewtschenko J. A., Wilkinson R. J., Baugh C. M., Pascoli S., 2014, MNRAS, 445, L31

Carlin J. L. et al., 2017, AJ, 154, 267

Cautun M., Hellwing W. A., van de Weygaert R., Frenk C. S., Jones B. J. T., Sawala T., 2014a, MNRAS, 445, 1820

Cautun M., Frenk C. S., van de Weygaert R., Hellwing W. A., Jones B. J. T., 2014b, MNRAS, 445, 2049

Crain R. A. et al., 2015, MNRAS, 450, 1937

D'Onghia E., Springel V., Hernquist L., Keres D., 2010, ApJ, 709, 1138

Davis M., Efstathiou G., Frenk C. S., White S. D. M., 1985, ApJ, 292

Drlica-Wagner A. et al., 2015, ApJ, 813, 109

Drlica-Wagner A. et al., 2016, ApJ, 833, L5

Einasto J., 1965, Trudy Inst. Astroz. Alma-Ata, 5, 87

Errani R., Peñarrubia J., Laporte C. F. P., Gómez F. A., 2017, MNRAS, 465, L59

Fattahi A. et al., 2016, MNRAS, 457, 844

Frenk C., White S., 2012, Ann. Phys., 524, 507

Garrison-Kimmel S. et al., 2017, MNRAS, 471, 1709

Guo Q., Cole S., Eke V., Frenk C., 2012, MNRAS, 427, 428

Han J., Cole S., Frenk C. S., Jing Y., 2016, MNRAS, 457, 1208

Hargis J. R., Willman B., Peter A. H. G., 2014, ApJ, 795, L13

Hellwing W. A., Frenk C. S., Cautun M., Bose S., Helly J., Jenkins A., Sawala T., Cytowski M., 2016, MNRAS, 457, 3492

Homma D. et al., 2016, ApJ, 832, 21

Homma D. et al., 2018, PASJ, 70

Hunter J. D., 2007, Computing in Science & Engineering, 9, 3, 90

Jethwa P., Erkal D., Belokurov V., 2016, MNRAS, 461, 2212

Jethwa P., Erkal D., Belokurov V., 2018, MNRAS, 473, 2060

Jones E., Oliphant T., Peterson P., 2011, SciPy: Open source scientific tools for Python, available at: www.scipy.org

Kallivayalil N., van der Marel R. P., Besla G., Anderson J., Alcock C., 2013, ApJ, 764, 161

Kennedy R., Frenk C., Cole S., Benson A., 2014, MNRAS, 442, 2487

Kim D., Jerjen H., Mackey D., Costa G. S. D., Milone A. P., 2015, ApJ, 804, L44

Kim D. et al., 2016, ApJ, 833, 16

Klypin A., Kravtsov A. V., Valenzuela O., Prada F., 1999, ApJ, 522, 82

Koposov S. et al., 2008, ApJ, 686, 279

Koposov S. E., Belokurov V., Torrealba G., Evans N. W., 2015a, ApJ, 805, 130

Koposov S. E. et al., 2015b, ApJ, 811, 62

Kuhlen M., Diemand J., Madau P., Zemp M., 2008, J. Phys.: Conf. Ser., 125, 012008

Lacey C. G. et al., 2016, MNRAS, 462, 3854

Laevens B. P. M. et al., 2015, ApJ, 813, 44

Li T. S. et al., 2017, ApJ, 838, 8

Libeskind N. I., Frenk C. S., Cole S., Helly J. C., Jenkins A., Navarro J. F., Power C., 2005, MNRAS, 363, 146

Lovell M. R. et al., 2012, MNRAS, 420, 2318

Lovell M. R., Frenk C. S., Eke V. R., Jenkins A., Gao L., Theuns T., 2014, MNRAS, 439, 300

Lovell M. R. et al., 2017, MNRAS, 468, 4285

Ludlow A. D., Bose S., Angulo R. E., Wang L., Hellwing W. A., Navarro J. F., Cole S., Frenk C. S., 2016, MNRAS, 460, 1214

Macciò A. V., Fontanot F., 2010, MNRAS, 404, L16

Macciò A. V., Dutton A. A., Bosch V. D. C F., Moore B., Potter D., Stadel J., 2007, MNRAS, 378, 55

Marsh D. J. E., 2016, Phys. Rep., 643, 1

Martin N. F. et al., 2015, ApJ, 804, L5

McConnachie A. W., 2012, AJ, 144, 4

Merritt D., Graham A. W., Moore B., Diemand J., Terzić B., 2006, AJ, 132, 2685

Moore B., Ghigna S., Governato F., Lake G., Quinn T., Stadel J., Tozzi P., 1999, ApJ, 524, L19

Navarro J. F., Frenk C. S., White S. D. M., 1995, MNRAS, 275, 720

Navarro J. F., Frenk C. S., White S. D. M., 1996, ApJ, 462, 563

Navarro J. F., Frenk C. S., White S. D. M., 1997, ApJ, 490, 493

Navarro J. F. et al., 2004, MNRAS, 349, 1039

Newton O., Cautun M., 2018, MW Satellite LF: V1.0.0, doi:10.5281/zenodo.1205622

Okamoto T., Eke V. R., Frenk C. S., Jenkins A., 2005, MNRAS, 363, 1299

Onions J. et al., 2012, MNRAS, 423, 1200

Peebles P. J. E., 1982, ApJ, 263, L1

Piffl T. et al., 2014, A&A, 562, A91

Polisensky E., Ricotti M., 2011, Phys. Rev. D, 83, 043506

Sales L. V., Navarro J. F., Lambas D. G., White S. D. M., Croton D. J., 2007, MNRAS, 382, 1901

Sales L. V., Navarro J. F., Cooper A. P., White S. D. M., Frenk C. S., Helmi A., 2011, MNRAS, 418, 648

Sawala T. et al., 2015, MNRAS, 448, 2941

Sawala T. et al., 2016a, MNRAS, 456, 85

Sawala T. et al., 2016b, MNRAS, 457, 1931

Sawala T., Pihajoki P., Johansson P. H., Frenk C. S., Navarro J. F., Oman K. A., White S. D. M., 2017, MNRAS, 467, 4383

Schaye J. et al., 2015, MNRAS, 446, 521

Schewtschenko J. A., Wilkinson R. J., Baugh C. M., Bœhm C., Pascoli S., 2015, MNRAS, 449, 3587

Schneider A., 2016, J. Cosmol. Astropart. Phys., 2016, 059

Shao S., Cautun M., Frenk C. S., Gao L., Crain R. A., Schaller M., Schaye J., Theuns T., 2016, MNRAS, 460, 3772

Shen S., Madau P., Conroy C., Governato F., Mayer L., 2014, ApJ, 792, 99

Simha V., Cole S., 2017, MNRAS, 472, 1392

Somerville R. S., 2002, ApJ, 572, L23

Spergel D. N. et al., 2003, ApJS, 148, 175

Springel V. et al., 2008, MNRAS, 391, 1685

Tollerud E. J., Bullock J. S., Strigari L. E., Willman B., 2008, ApJ, 688, 277

Torrealba G., Koposov S. E., Belokurov V., Irwin M., 2016a, MNRAS, 459, 2370

Torrealba G. et al., 2016b, MNRAS, 463, 712

Torrealba G. et al., 2018, MNRAS, 475, 5085

van der Walt S., Colbert S. C., Varoquaux G., 2011, Computing in Science & Engineering, 13, 22

Walker M. G. et al., 2016, ApJ, 819, 53

Walsh S. M., Willman B., Jerjen H., 2009, AJ, 137, 450

Wang W., White S. D. M., 2012, MNRAS, 424, 2574

Wang J., Frenk C. S., Navarro J. F., Gao L., Sawala T., 2012, MNRAS, 424, 2715

Wang J., Frenk C. S., Cooper A. P., 2013, MNRAS, 429, 1502

Wang W., Han J., Cooper A. P., Cole S., Frenk C., Lowing B., 2015, MNRAS, 453, 377

Watkins L. L. et al., 2009, MNRAS, 398, 1757

Weinberg D. H., Bullock J. S., Governato F., de Naray R. K., Peter A. H. G., 2015, PNAS, 112, 12249

Wheeler C., Oñorbe J., Bullock J. S., Boylan-Kolchin M., Elbert O. D., Garrison-Kimmel S., Hopkins P. F., Kereš D., 2015, MNRAS, 453, 1305

APPENDIX A: TABLES OF KNOWN SATELLITE GALAXIES

Table A1. Known MW satellite galaxies identified in surveys used in this analysis, grouped according to the survey in which they were detected. For each satellite we provide its absolute *V*-band magnitude, M_V, heliocentric distance, $D_\odot$, and – for DES satellites – its probability of association with the LMC.

Satellite	M_V	$D_\odot$ (kpc)	p^a_{LMC}	Reference[e]
Classical				
Carina	− 9.1	105		
Draco I	− 8.8	76		
Fornax	− 13.4	147		
Leo I	− 12.0	254		
Leo II	− 9.8	233		
LMC	− 18.1	51		
Ursa Minor	− 8.8	76		
SMC	− 16.8	64		
Sculptor	− 11.1	86		
Sextans	− 9.3	86		
Sagittarius I	− 13.5	26		
SDSS DR9				
Boötes I	− 6.3	66		
Boötes II	− 2.7	42		
Canes Venatici I	− 8.6	218		
Canes Venatici II	− 4.9	160		
Coma	− 4.1	44		
Hercules	− 6.6	132		
Leo IV	− 5.8	154		
Leo V	− 5.2	178		
Leo T	− 8.0	417		
Pegasus III	− 3.4	215		(1)
Pisces I[b]	...	80		(2)
Pisces II	− 5.0	182		
Segue I	− 1.5	23		
Segue II	− 2.5	35		
Ursa Major I	− 5.5	97		
Ursa Major II	− 4.2	32		
Willman I	− 2.7	38		
DES				
Cetus II[c]	0.0	30	0.00^d	(3)
Columba I	− 4.2	183	0.11	(4)
Eridanus II	− 7.1	366	0.00^d	(5)
Eridanus III[c]	− 2.4	95	0.00^d	(3)
Grus I[c]	− 3.4	120	0.64	(3)
Grus II[c]	− 3.9	53	0.57	(3)
Horologium I	− 3.5	87	0.79	(3,6)
Horologium II[c]	− 2.6	78	0.80	(3)
Indus II[c]	− 4.3	214	0.19	(3)
Phoenix II[c]	− 3.7	95	0.75	(3)
Pictoris[c]	− 3.7	126	0.62	(3)
Reticulum II	− 3.6	32	0.75	(3,6)
Reticulum III[c]	− 3.3	92	0.58	(3)
Tucana II	− 3.9	58	0.75	(3,7)
Tucana III[c]	− 2.4	25	0.52	(3)
Tucana IV[c]	− 3.5	48	0.79	(3)
Tucana V[c]	− 1.6	55	0.81	(3)

Notes. [a]Obtained from Jethwa et al. (2016, fig. 9).
[b]The method of detection was different from that applied to other satellites in the SDSS.
[c]Not spectroscopically confirmed.
[d]No probability of association with LMC provided.
[e]Data reproduced from McConnachie (2012, tables 2 and 3) unless indicated otherwise: (1) Kim et al. (2015, 2016), (2) Watkins et al. (2009), (3) Drlica-Wagner et al. (2015, Table 4), (4) Carlin et al. (2017), (5) Li et al. (2017), (6) Koposov et al. (2015b), and (7) Walker et al. (2016).

Table A2. Known MW satellite galaxies identified in surveys *not* used in this analysis, grouped according to the survey in which they were detected. We provide the same data for each satellite as described in Table A1.

Satellite	M_V	$D_\odot$ (kpc)	Reference[b]
VLT ATLAS			
Aquarius II	− 4.2	108	(1)
Crater II	− 8.2	118	(2)
Pan-STARRS			
Draco II	− 2.9	20	(3)
Sagittarius II[a]	− 5.2	67	(3)
Triangulum II	− 1.2	28	(4)
SMASH			
Hydra II	− 4.8	134	(5)
HSC			
Virgo I[a]	− 0.3	91	(6)
Cetus III[a]	− 2.4	251	(7)
MagLiteS			
Carina II	− 4.5	37	(8)
Carina III[a]	− 2.4	28	(8)
Pictoris II[a]	− 3.2	45	(9)

Notes. [a]Not spectroscopically confirmed.
[b]Data reproduced from (1) Torrealba et al. (2016b), (2) Torrealba et al. (2016a), (3) Laevens et al. (2015), (4) Carlin et al. (2017), (5) Martin et al. (2015), (6) Homma et al. (2016), (7) Homma et al. (2018), (8) Torrealba et al. (2018), and (9) Drlica-Wagner et al. (2016).

APPENDIX B: EFFECTS OF RESOLUTION

In this Appendix we provide details of the scheme that we implement to supplement the $z = 0$ subhalo population of each AQUARIUS halo with subhaloes that are otherwise unresolved at this time. We also compare the difference these additions make to the subhalo number density profile.

The semi-analytic model GALFORM described by Lacey et al. (2016), which is based on the same cosmology as the AQUARIUS simulation suite, is applied to each of the AQUARIUS DM haloes in turn. We use the Simha & Cole (2017) merging scheme to track the dynamical evolution of subhaloes over the course of cosmic time. Well-resolved subhaloes are tracked directly by the *N*-body simulation; however, those that fall below the resolution limit are lost. Simha & Cole recover this population by tracking the most bound particle in these subhaloes from the last epoch at which they were associated with a resolved subhalo. They then remove subhaloes from this population if one of the following criteria is satisfied:

(i) A time has elapsed after the last epoch at which the subhalo was resolved, which is equal to or greater than the dynamical friction timescale.

(ii) The subhalo passes within the halo tidal disruption radius at any time.

In both of the above cases the effects of tidal stripping on the subhalo are ignored, as are interactions between orbiting subhaloes.

In Fig. B1 we compare the normalized cumulative radial subhalo counts of the AQUARIUS A1 and A2 haloes with the $v_{peak} \geq 10\,km\,s^{-1}$ selection threshold applied. Prior to the application of GALFORM the original normalized subhalo counts are highly discrepant in the inner regions of the haloes. The spread in the predicted counts at $M_V = 0$ in Aq-A1 and Aq-A2 is also wider than the spread in the predictions from the other L2 haloes (B2-E2). When correcting for the 'orphan' population, which is very centrally concentrated, the discrepancy in the Aq-A1 and Aq-A2 normalized subhalo counts is
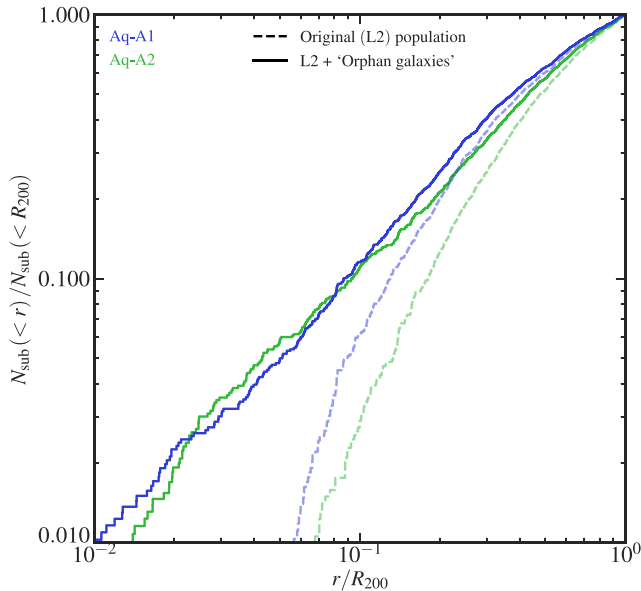
Figure B1. Normalized cumulative subhalo number counts for the Aq-A1 and Aq-A2 haloes. The dashed lines show the original, uncorrected number counts prior to the application of GALFORM. The solid lines show the number counts for each halo after adding 'orphan galaxies' to the original population. The subhalo populations before the correction are poorly sampled in the innermost regions, and are not well-converged between the two haloes.

almost completely eliminated. As a result the spread in the $M_V = 0$ predictions is also reduced such that it is much smaller than the spread in the predictions from the other 'L2 + orphans' haloes. The spread in these latter predictions is also significantly reduced by the correction, which shows that failing to account for this artificially inflates the halo-to-halo scatter.

APPENDIX C: BARYONIC EFFECTS

D'Onghia et al. (2010), Sawala et al. (2017), and Garrison-Kimmel et al. (2017) identify systematic differences in the subhalo radial number density profiles of haloes in DM-only and hydrodynamic simulations. The enhanced tidal stripping by the central baryonic disc leads to a reduction in the number of subhaloes in hydrodynamic simulations compared to their DM-only counterparts. The subhalo depletion is a radially varying function that peaks in the innermost regions of the host halo.

The subhalo number density profiles can be fit using a double power-law functional form, which is given in Sawala et al. (2017, equation 2). With help from Till Sawala (private communication), we determined that some of the values stated for the fitting parameters of equation (2) in the published version of the paper are incorrect. Taking the raw data from Till Sawala, we made our own fits, binning the data in units of $\chi = r / R_{200}$. Fig. C1 gives the averaged subhalo number density profiles of 4 MW-like haloes from the APOSTLE suite. To improve our statistics, we also average over 5 Gyr of cosmic time, similar to Sawala et al. To these profiles, we fit a double power law of the form

$$\rho(r) = 2^{(\beta-\gamma)/\alpha} \rho_s (c_{200}\chi)^{-\gamma} (1 + [c_{200}\chi]^\alpha)^{(\gamma-\beta)/\alpha}, \qquad (C1)$$

which gives fitting parameters of

$$(c_{200}, \rho_s, \alpha, \beta, \gamma) = (2.50, 875, 4.41, 1.80, 0.613)$$
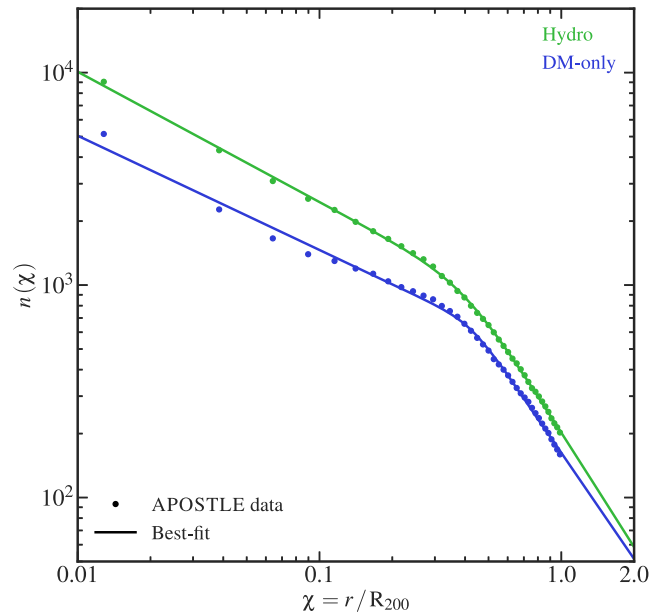

Figure C1. Fits to subhalo number density profiles in DM-only and hydrodynamic simulations. The points show averaged radial profiles for four APOSTLE haloes. To obtain better statistics, these points were also averaged over 5 Gyr of cosmic time; see Sawala et al. (2017) for details. The solid lines show the best-fitting double power laws (see the main text for the best-fitting parameters).

and

$$(c_{200}, \rho_s, \alpha, \beta, \gamma) = (2.35, 613, 8.35, 1.66, 0.537)$$

for the DM-only and hydrodynamic simulations, respectively.

These fits are only constrained in the radial range $[0.01, 1.0]\,\chi$ but in practice we extrapolate the profiles over a slightly wider range of $[10^{-3}, 2.0]\,\chi$ to subsample our haloes. We find that only minimal extrapolation is required to achieve this, and that the ratio in this extended range is also slowly varying.

The subhalo depletion is given by the ratio between the hydrodynamic and DM-only subhalo number density profiles. We compute this using the best-fitting double power-law fits given above. The ratio varies from ∼0.5 for the inner halo to about ∼0.8 at R_{200}. We correct the AQUARIUS subhalo distributions using this depletion value. For each subhalo, we compute the subhalo depletion value at its radial position and use a Monte Carlo approach to decide if this subhalo is retained or discarded. Only retained subhaloes are used as input to the Bayesian inference method.

APPENDIX D: TESTING PREVIOUS METHODS

Here, we test the T08 method by applying it to a set of mock satellite observations. This is similar to the exercise in Section 3.2.2, where, using the same blind mock observations, we demonstrated that the Bayesian approach introduced in this paper successfully infers the input 'true' luminosity function used to generate the mock observations.

A set of 100 mock SDSS observations was generated from a 'true' population by one of the authors (MC; see Section 3.2.2 for a description of the mocks) and supplied to another (ON), who applied the T08 method. In order to return an unbiased estimate, we applied the T08 approach using a completeness radius that corresponds to a detection efficiency, $\epsilon = 0.5$, and used as input only
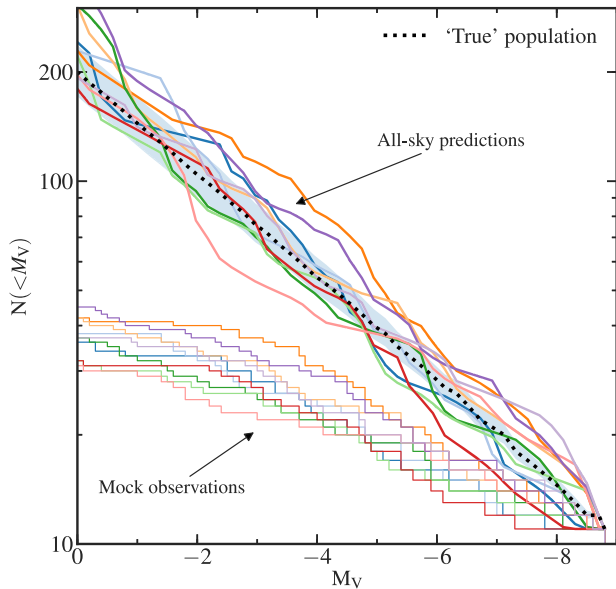
Figure D1. Test of the T08 method using mock observations. The thick dotted line shows the input luminosity function used to create the 10 SDSS mock observations, whose luminosity functions are shown as thin solid lines. Each of the mock observations was used, in turn, to predict a cumulative satellite luminosity function, with the corresponding results shown as thick solid lines. The shaded region represents the 68 per cent (statistical) uncertainty from one of the mocks, shifted to lie on top of the input luminosity function. The dashed lines bound the 68 per cent (statistical) confidence region over the medians of all 100 mock predictions.

those observed satellites with detection efficiencies, $\epsilon \geq 0.5$. Using a random sample of 10 mock observations, we compare in Fig. D1 the scatter among the various mocks with the typical error of the T08 method. We find that the typical 68 per cent (statistical) uncertainty range estimated by the T08 method is too low: for most magnitude values, most of the 10 mocks are outside the 68 per cent (statisti-

cal) confidence interval. This was also demonstrated in Fig. 5 and arises because the T08 method does not incorporate the effects of stochasticity into its estimation of the uncertainties.

APPENDIX E: DATA TABLE

Table E1. Cumulative number of satellites as a function of absolute magnitude within a heliocentric distance of 300 kpc for a $1.0 \times 10^{12}\,M_\odot$ MW halo, inferred from a Bayesian analysis of the SDSS DR9 + DES observed satellites. The cumulative number of these observed satellites is provided for reference. The quoted confidence limits are for statistical errors only.

| M_V | $N(<M_V)$ | | Confidence limits: lower–upper | | |
	Observed	Predicted	68%	95%	98%
−8.8	11	11	–	–	–
−8.5	12	13	12–15	12–19	12–21
−8.0	12	14	13–16	12–20	12–21
−7.5	12	15	13–17	13–21	13–22
−7.0	12	15	14–17	13–21	13–23
−6.5	13	16	14–19	13–23	13–25
−6.0	14	19	16–22	15–27	15–30
−5.5	16	22	19–26	17–32	16–34
−5.0	18	27	23–32	20–39	20–43
−4.5	20	31	27–38	23–47	22–50
−4.0	23	41	35–49	30–60	29–64
−3.5	30	52	44–62	39–76	37–82
−3.0	33	61	51–73	44–89	43–95
−2.5	37	77	64–93	55–114	52–123
−2.0	39	89	74–108	63–133	60–142
−1.5	41	96	79–118	67–147	63–158
−1.0	41	105	86–131	72–163	68–175
−0.5	41	115	92–146	75–186	71–203
0.0	42	124	97–164	78–225	73–249

This paper has been typeset from a TEX/LATEX file prepared by the author.